

Banner appropriate to article type will appear here in typeset article

1 **The production of uncertainty in three-dimensional** 2 **Navier-Stokes turbulence**

3 **Jin Ge¹†, Joran Rolland¹‡ and John Christos Vassilicos¹¶**

4 ¹Univ. Lille, CNRS, ONERA, Arts et Métiers ParisTech, Centrale Lille, UMR 9014 - LMFL - Laboratoire
5 de Mécanique des Fluides de Lille - Kampé de Fériet, F-59000 Lille, France

6 (Received xx; revised xx; accepted xx)

7 We derive the evolution equation of the average uncertainty energy for periodic/homogeneous
8 incompressible Navier-Stokes turbulence and show that uncertainty is increased by strain
9 rate compression and decreased by strain rate stretching. We use three different direct
10 numerical simulations (DNS) of non-decaying periodic turbulence and identify a similarity
11 regime where (a) the production and dissipation rates of uncertainty grow together in
12 time, (b) the parts of the uncertainty production rate accountable to average strain rate
13 properties on the one hand and fluctuating strain rate properties on the other also grow
14 together in time, (c) the average uncertainty energies along the three different strain rate
15 principal axes remain constant as a ratio of the total average uncertainty energy, (d) the
16 uncertainty energy spectrum's evolution is self-similar if normalised by the uncertainty's
17 average uncertainty energy and characteristic length and (e) the uncertainty production rate
18 is extremely intermittent and skewed towards extreme compression events even though the
19 most likely uncertainty production rate is zero. Properties (a), (b) and (c) imply that the
20 average uncertainty energy grows exponentially in this similarity time range. The Lyapunov
21 exponent depends on both the Kolmogorov time scale and the smallest Eulerian time scale,
22 indicating a dependence on random large-scale sweeping of dissipative eddies. In the two
23 DNS cases of statistically stationary turbulence, this exponential growth is followed by an
24 exponential of exponential growth, which is in turn followed by a linear growth in the one
25 DNS case where the Navier-Stokes forcing also produces uncertainty.

26 **Key words:**

27 **1. Introduction**

28 It is basic textbook knowledge that turbulent flow realisations are not repeatable whereas
29 statistics over many realisations of a turbulent flow are (Tennekes & Lumley 1972). This
30 well-known empirical observation suggests the presence of some kind of chaotic attractor.
31 The pioneering work of Lorenz has shown the presence of chaos and strange attractors and

† Email address for correspondence: jin.ge@centrale.centralelille.fr

‡ Email address for correspondence: joran.rolland@centralelille.fr

¶ Email address for correspondence: john-christos.vassilicos@centralelille.fr

32 their resulting high sensitivity to initial conditions in non-linear systems with a small number
 33 of degrees of freedom (Lorenz 1963; Sparrow 2012). Deissler (1986) demonstrated that
 34 similar extreme sensitivity to initial conditions is also present in fully developed turbulent
 35 solutions of the Navier-Stokes equation which is a non-linear system with a very large number
 36 of degrees of freedom, in fact asymptotically infinite with increasing Reynolds number. High
 37 sensitivity to initial conditions is at the root of non-repeatability and therefore uncertainty.
 38 Uncertainty is present in a wide range of non-linear systems with many degrees of freedom
 39 such as turbulent flows, magnetohydrodynamics (Ho *et al.* 2020) and plasma physics (Cheung
 40 & Wong 1987) and is also at the core of the problem of atmospheric predictability (Lorenz
 41 1963; Leith 1971). It may not be enough, however, to simply rely on the general concepts of
 42 chaos and strange attractors (and bifurcations) if one wants to understand uncertainty. This
 43 paper's motivation is to understand uncertainty and its growth in the case of Navier-Stokes
 44 turbulence in some physically concrete terms.

45 The solutions of the Navier-Stokes equation are velocity and pressure fields which evolve
 46 in time. The uncertainty of a time-dependent velocity field $\mathbf{u}^{(1)}(\mathbf{x}, t)$ is measured by its
 47 difference from a velocity field $\mathbf{u}^{(2)}(\mathbf{x}, t)$ with near-identical initial conditions: the velocity
 48 difference between these two fields at time t is $\Delta\mathbf{u} \equiv \mathbf{u}^{(2)} - \mathbf{u}^{(1)}$. Based on this velocity-
 49 difference field, the average uncertainty in the system is measured in terms of its kinetic
 50 energy as $\langle E_\Delta \rangle \equiv \langle |\Delta\mathbf{u}|^2 / 2 \rangle$, where $\langle \cdot \rangle$ represents spatial average (over \mathbf{x}). In the presence
 51 of a strange attractor, its chaotic nature is expected to lead to exponential growth of the
 52 difference between two fields initially very close together (Deissler 1986; Ruelle 1981), i.e.

$$53 \quad \frac{d}{dt} \langle E_\Delta \rangle = 2\lambda \langle E_\Delta \rangle, \quad (1.1)$$

54 where λ is the maximal Lyapunov exponent.

55 To evaluate the Lyapunov exponent in the case of statistically stationary homogeneous
 56 turbulence, Ruelle (1979) argued that when the two fields $\mathbf{u}^{(1)}$ and $\mathbf{u}^{(2)}$ differ initially
 57 only at the very smallest scales, then λ^{-1} should be the Kolmogorov time scale τ_η i.e.
 58 $\lambda^{-1} \sim \tau_\eta \equiv (\nu/\varepsilon)^{1/2}$ where ν is the fluid's kinematic viscosity and ε is the turbulence
 59 dissipation rate. Kolmogorov equilibrium $\varepsilon \sim U^3/L$ for statistically stationary homogeneous
 60 turbulence implies $\lambda \sim \tau_\eta^{-1} \sim (L/U)^{-1} \text{Re}^{1/2}$ in terms of the large eddy turnover time L/U and
 61 the Reynolds number $\text{Re} = UL/\nu$ where U is the rms turbulence velocity and L the integral
 62 length scale. Intermittency corrections have been considered in the form $\lambda \sim (L/U)^{-1} \text{Re}^a$
 63 where $a = 0.459$ instead of 0.5 (Crisanti *et al.* (1993) derived this correction on the basis of
 64 a multi-fractal model). Whilst this correction agrees with numerical observations from the
 65 shell model (Aurell *et al.* 1997), neither $a = 0.459$ nor $a = 0.5$ agree with observations from
 66 direct numerical simulations (DNS) of Navier-Stokes statistically stationary homogeneous
 67 turbulence (Berera & Ho 2018; Boffetta & Musacchio 2017). In fact, the DNS results
 68 of Mohan *et al.* (2017) suggest that $\lambda\tau_\eta$ increases with Reynolds number, i.e. $a > 0.5$,
 69 suggesting that time scales smaller than τ_η may be at play. Understanding the growth of
 70 uncertainty in some physically concrete terms, as stated above, must also involve shedding
 71 some light on the scalings of the maximal Lyapunov exponent which clearly remains an
 72 open question. In fact the question may be even more widely open as a superfast uncertainty
 73 growth may have been observed at very early times in some DNS results (Li *et al.* 2020). Such
 74 superfast growth is not ruled out by the rigorous constraint on the uncertainty growth derived
 75 from the Navier-Stokes equation by Li (2014): $\langle E_\Delta(t) \rangle / \langle E_\Delta(0) \rangle \leq \exp(\sigma\sqrt{\text{Re}}\sqrt{t} + \sigma_1 t)$
 76 where σ and σ_1 are the coefficients depending on the perturbations.

77 The difference between the velocity fields $\mathbf{u}^{(1)}$ and $\mathbf{u}^{(2)}$ may be expected to grow in a
 78 way that develops differences over length scales l larger than the very smallest scales. When

79 this happens, one may assume equation (1.1) to remain valid but with a maximal Lyapunov
 80 exponent which reflects the characteristic time at length scale l , i.e. $\lambda^{-1} \sim \tau_l \equiv E_l/\varepsilon$ where
 81 E_l is the kinetic energy characterising length scale l (Lorenz 1969). It may then be natural to
 82 expect $\langle E_\Delta \rangle \sim E_l$ (Aurell *et al.* 1997) which leads to a linear growth of $\langle E_\Delta \rangle$ from equation
 83 (1.1) and $\lambda^{-1} \sim E_l/\varepsilon$. A linear growth has been widely reported in numerical experiments
 84 using the Eddy Damped Quasi-Normal Markovian (EDQNM) closure (Leith & Kraichnan
 85 1972), shell models (Aurell *et al.* 1997) and DNS (Berera & Ho 2018; Boffetta & Musacchio
 86 2017).

87 There have already been some attempts at understanding uncertainty in physically concrete
 88 terms. Boffetta *et al.* (1997) investigated the growth of uncertainty in two-dimensional
 89 decaying homogeneous turbulence and found that the uncertainty growth is ruled by the
 90 error located in the positions of vortices. Mohan *et al.* (2017) found that much or most of
 91 the uncertainty is concentrated near vortex tubes in three-dimensional statistically stationary
 92 homogeneous turbulence and considered the possibility of local instability mechanisms
 93 reminiscent of pairing instabilities of corotating vortices as in mixing layers. Clark *et al.*
 94 (2021, 2022) investigated the dependence of uncertainty on spatial dimension (between 2
 95 to 8) in DNS and in an EDQNM model of statistically stationary homogeneous turbulence.
 96 They found a critical dimension $d_c \approx 5.88$ which is close to the dimension of maximum
 97 enstrophy production and above which the turbulence uncertainty is no longer ruled by
 98 chaoticity. From these results, Clark *et al.* (2022) speculated that vortex stretching and strain
 99 self-amplification, which are responsible for enstrophy generation, may also be important
 100 for uncertainty generation. The present paper is an effort in the direction of understanding
 101 uncertainty growth in terms of vortex stretching and compression dynamics and statistics.

102 In the following section we derive, from the Navier-Stokes equations, the evolution
 103 equation for the uncertainty energy $\langle E_\Delta \rangle$ in the case of periodic/homogeneous turbulence.
 104 This uncertainty equation involves three different mechanisms: internal production resulting
 105 from interactions between the strain rate and the velocity-difference field, dissipation of
 106 the velocity-difference field and external force input. We use three different DNS of forced
 107 periodic/homogeneous turbulence to study these mechanisms and in section 3 we present
 108 their numerical setups. Our DNS results and their analysis are presented in section 4 and we
 109 conclude in section 5.

110 2. Theoretical analysis of the uncertainty

111 In the first part of this section we derive the evolution equation for the uncertainty energy
 112 $\langle E_\Delta \rangle$ and in the second part we discuss the production of uncertainty energy.

113 2.1. Evolution equation of uncertainty

114 The reference field $\mathbf{u}^{(1)}$ and the perturbed field $\mathbf{u}^{(2)} = \mathbf{u}^{(1)} + \Delta\mathbf{u}$ are both governed by the
 115 incompressible Navier-Stokes equations

$$116 \quad \frac{\partial}{\partial t} u_i^{(m)} + u_j^{(m)} \frac{\partial}{\partial x_j} u_i^{(m)} = -\frac{\partial}{\partial x_i} p^{(m)} + \nu \frac{\partial^2}{\partial x_j \partial x_j} u_i^{(m)} + f_i^{(m)}, \quad (2.1)$$

$$\frac{\partial}{\partial x_i} u_i^{(m)} = 0,$$

117 where p is the pressure to density ratio, $\mathbf{f} = (f_1, f_2, f_3)$ is the force per unit mass field, and
 118 the number $m = 1$ or 2 in the superscript parentheses indicates whether the velocity/pressure

119 field is the reference or the perturbed one. The equation for $\Delta \mathbf{u} \equiv \mathbf{u}^{(2)} - \mathbf{u}^{(1)}$ follows and is

$$120 \quad \frac{\partial}{\partial t} \Delta u_i + u_j^{(1)} \frac{\partial}{\partial x_j} \Delta u_i + \Delta u_j \frac{\partial}{\partial x_j} \Delta u_i + \Delta u_j \frac{\partial}{\partial x_j} u_i^{(1)} = - \frac{\partial}{\partial x_i} \Delta p + \nu \frac{\partial^2}{\partial x_j \partial x_j} \Delta u_i + \Delta f_i, \quad (2.2)$$

$$\frac{\partial}{\partial x_i} \Delta u_i = 0,$$

121 where $\Delta p \equiv p^{(2)} - p^{(1)}$ and $\Delta \mathbf{f} \equiv \mathbf{f}^{(2)} - \mathbf{f}^{(1)}$ are the pressure and forcing differences
 122 respectively. The divergence-free property of $\mathbf{u}^{(m)}$ implies that $\Delta \mathbf{u}$ is also divergence-free.
 123 Multiplying both sides of equation (2.2) with Δu_i , summing over $i = 1, 2, 3$ and using
 124 incompressibility we obtain

$$125 \quad \frac{\partial}{\partial t} E_\Delta + \frac{\partial}{\partial x_j} \left(u_j^{(1)} E_\Delta \right) + \frac{\partial}{\partial x_j} \left(\Delta u_j E_\Delta \right) + \Delta u_i \Delta u_j \frac{\partial}{\partial x_j} u_i^{(1)} =$$

$$126 \quad - \frac{\partial}{\partial x_i} \left(\Delta u_i \Delta p \right) + \nu \frac{\partial}{\partial x_j} \left(\frac{\partial E_\Delta}{\partial x_j} \right) - \nu \frac{\partial \Delta u_i}{\partial x_j} \frac{\partial \Delta u_i}{\partial x_j} + \Delta f_i \Delta u_i. \quad (2.3)$$

127 The second and third terms on the left-hand side of equation (2.3), as well as the first and
 128 second terms on the right-hand side, are in flux form. In the case of periodic/homogeneous
 129 turbulence, these four terms average to zero when a spatial average is applied to them, and
 130 therefore equation (2.3) leads to

$$131 \quad \frac{d}{dt} \langle E_\Delta \rangle = \langle P_\Delta \rangle - \langle \varepsilon_\Delta \rangle + \langle F_\Delta \rangle, \quad (2.4)$$

132 where

$$P_\Delta = -\Delta u_i S_{ij}^{(1)} \Delta u_j, \quad \varepsilon_\Delta = \nu \frac{\partial \Delta u_i}{\partial x_j} \frac{\partial \Delta u_i}{\partial x_j}, \quad F_\Delta = \Delta f_i \Delta u_i \quad (2.5a, b, c)$$

133 and $S_{ij}^{(1)} = \left(\partial u_i^{(1)} / \partial x_j + \partial u_j^{(1)} / \partial x_i \right) / 2$ is the reference field's strain rate tensor.

134 In periodic/homogeneous turbulence the average uncertainty energy evolves via (i) dissipation
 135 of uncertainty which always reduces uncertainty because the dissipation rate ε_Δ is
 136 always positive, (ii) external input/output of uncertainty with rate F_Δ which depends on the
 137 force-difference field $\Delta \mathbf{f}$, and (iii) internal production of uncertainty via the production rate
 138 P_Δ . In the absence of external force difference (i.e. $\Delta \mathbf{f} = 0$), uncertainty can only grow
 139 because of internal production in which case $\langle P_\Delta \rangle$ should be positive and greater than $\langle \varepsilon_\Delta \rangle$.

140 Note that both fields $\mathbf{u}^{(1)}$ and $\mathbf{u}^{(2)}$ can be taken as the reference field and we therefore
 141 must have $\langle P_\Delta \rangle = - \left\langle \Delta u_i S_{ij}^{(1)} \Delta u_j \right\rangle = - \left\langle \Delta u_i S_{ij}^{(2)} \Delta u_j \right\rangle$ in periodic/homogeneous turbulence.

142 Indeed, defining $\Delta S_{ij} = \left(\partial \Delta u_i / \partial x_j + \partial \Delta u_j / \partial x_i \right) / 2$, we have $S_{ij}^{(2)} = S_{ij}^{(1)} + \Delta S_{ij}$ and $\langle P_\Delta \rangle =$
 143 $- \left\langle \Delta u_i S_{ij}^{(1)} \Delta u_j \right\rangle = - \left\langle \Delta u_i S_{ij}^{(2)} \Delta u_j \right\rangle - \left\langle \Delta u_i \Delta S_{ij} \Delta u_j \right\rangle$. Given that $\Delta \mathbf{u}$ is divergence-free, we

144 also have $\Delta u_i \Delta S_{ij} \Delta u_j = \frac{1}{2} \left(\frac{\partial}{\partial x_j} \left(\Delta u_j E_\Delta \right) + \frac{\partial}{\partial x_i} \left(\Delta u_i E_\Delta \right) \right)$ which implies $\left\langle \Delta u_i \Delta S_{ij} \Delta u_j \right\rangle = 0$

145 for periodic/homogeneous turbulence. Hence, $\langle P_\Delta \rangle = - \left\langle \Delta u_i S_{ij}^{(1)} \Delta u_j \right\rangle = - \left\langle \Delta u_i S_{ij}^{(2)} \Delta u_j \right\rangle$.

146 2.2. Production of uncertainty

147 To consolidate the interpretation of P_Δ as internal production rate of uncertainty, we write

$$148 \quad E_\Delta + E_{\text{corr}} = E_{\text{tot}} \quad (2.6)$$

149 where $E_{\text{tot}} = E^{(1)} + E^{(2)} = \left(|\mathbf{u}^{(1)}|^2 + |\mathbf{u}^{(2)}|^2 \right) / 2$ and $E_{\text{corr}} = \mathbf{u}^{(1)} \cdot \mathbf{u}^{(2)}$. $\langle E_{\text{tot}} \rangle$ represents
 150 the average total kinetic energy of the reference and the perturbed velocity fields. Its rate of

151 change follows from equation (2.1) and is

$$152 \quad \frac{d}{dt} \langle E_{\text{tot}} \rangle = - \sum_{m=1}^2 \langle \varepsilon^{(m)} \rangle + \sum_{m=1}^2 \langle F^{(m)} \rangle, \quad (2.7)$$

153 where

$$\varepsilon^{(m)} \equiv \nu \frac{\partial u_i^{(m)}}{\partial x_j} \frac{\partial u_i^{(m)}}{\partial x_j}, \quad F^{(m)} \equiv f_i^{(m)} u_i^{(m)}. \quad (2.8a, b)$$

154 If the two velocity fields $\mathbf{u}^{(1)}$ and $\mathbf{u}^{(2)}$ are so perfectly correlated that they are identical,
 155 then $E_{\text{corr}} = E_{\text{tot}}$ and $E_{\Delta} = 0$. If, however, these two velocity fields are totally uncorrelated,
 156 then $\langle E_{\text{corr}} \rangle = 0$ and $\langle E_{\Delta} \rangle = \langle E_{\text{tot}} \rangle$. The average internal production rate of uncertainty $\langle P_{\Delta} \rangle$
 157 is an internal transfer rate between $\langle E_{\text{corr}} \rangle$ and $\langle E_{\Delta} \rangle$, i.e. a transfer rate from correlation to
 158 decorrelation if it is positive and from decorrelation to correlation if it is negative. Indeed,
 159 from equations (2.6), (2.7) and (2.4), we have

$$160 \quad \frac{d}{dt} \langle E_{\text{corr}} \rangle = - \langle P_{\Delta} \rangle - \langle \varepsilon_{\text{corr}} \rangle + \langle F_{\text{corr}} \rangle, \quad (2.9)$$

161 where

$$\varepsilon_{\text{corr}} = \nu \frac{\partial u_i^{(1)}}{\partial x_j} \frac{\partial u_i^{(2)}}{\partial x_j}, \quad F_{\text{corr}} = f_i^{(1)} u_i^{(2)} + f_i^{(2)} u_i^{(1)}. \quad (2.10a, b)$$

162 so that $\langle P_{\Delta} \rangle$ appears with opposite signs in equation (2.4) and in equation (2.9) and is absent
 163 from equation (2.7). If the two flows are identical, i.e. $\mathbf{u}^{(1)} = \mathbf{u}^{(2)}$, then $P_{\Delta} = \varepsilon_{\Delta} = F_{\Delta} = 0$,
 164 and if they are totally uncorrelated, then $\langle P_{\Delta} \rangle = \langle \varepsilon_{\text{corr}} \rangle = \langle F_{\text{corr}} \rangle = 0$.

165 According to equation (2.4), the evolution of the average uncertainty energy depends on the
 166 reference field via its strain rate tensor in the uncertainty production term. The incompressible
 167 Navier-Stokes evolution of the strain rate tensor is given by

$$168 \quad \frac{\partial}{\partial t} S_{ij} + u_k \frac{\partial}{\partial x_k} S_{ij} = -S_{ik} S_{kj} - \frac{1}{4} \left(\omega_i \omega_j - \delta_{ij} |\boldsymbol{\omega}|^2 \right) - P_{ij} + \nu \frac{\partial^2}{\partial x_j \partial x_j} S_{ij} + F_{ij}, \quad (2.11)$$

169 where $\boldsymbol{\omega} \equiv \nabla \times \mathbf{u}$ is the vorticity, δ_{ij} is the Kronecker delta, $P_{ij} \equiv \partial^2 p / \partial x_i \partial x_j$ is the pressure
 170 Hessian tensor and $F_{ij} \equiv (\partial f_i / \partial x_j + \partial f_j / \partial x_i) / 2$. The first and second terms in the right-hand
 171 side of equation (2.11) represent strain self-amplification and vortex-stretching respectively.
 172 They enhance the flow's strain rate once and where it is non-negligibly present, while the
 173 pressure Hessian induces its initial growth where it is negligibly small but contributes less to
 174 its further development (Paul *et al.* 2017). Therefore, the internal production of uncertainty
 175 can be related to the strain self-amplification and vortex-stretching as speculated by Clark
 176 *et al.* (2022) in their conclusion, but also to the pressure Hessian. F_{ij} in equation (2.11)
 177 represents the influence of the external forcing on the strain rate tensor. If the external forcing
 178 and its spatial gradients are not zero but there is no force difference in the system, i.e., $\Delta \mathbf{f} = 0$
 179 and therefore $F_{\Delta} = 0$, then there is no direct external generation or depletion of uncertainty
 180 in equation (2.4) but the external forcing does nevertheless influence the strain rate tensor's
 181 evolution because of F_{ij} in equation (2.11) and thereby indirectly influences the evolution of
 182 the internal production of uncertainty in equation (2.4).

183 The presence of the strain rate tensor in the internal uncertainty production reveals the
 184 critical and opposing roles of compression and stretching motions in the generation and
 185 reduction of uncertainty. Using the principal axes of $S_{ij}^{(1)}$ (or $S_{ij}^{(2)}$) as a local orthonormal

186 reference frame, we can write

$$187 \quad P_{\Delta} = - \left(\Lambda_1^{(1)} \Delta w_1^2 + \Lambda_2^{(1)} \Delta w_2^2 + \Lambda_3^{(1)} \Delta w_3^2 \right), \quad (2.12)$$

188 where $\Lambda_1^{(1)}, \Lambda_2^{(1)}, \Lambda_3^{(1)}$ are the eigenvalues of $S_{ij}^{(1)}$ and $\Delta w_1, \Delta w_2, \Delta w_3$ are the components of
 189 the velocity-difference vector projected on the corresponding principal axes. Incompressibil-
 190 ity forces $S_{ij}^{(1)}$ to be traceless, i.e., $\Lambda_1^{(1)} + \Lambda_2^{(1)} + \Lambda_3^{(1)} = 0$. Defining the order of eigenvalues
 191 as $\Lambda_1^{(1)} \leq \Lambda_2^{(1)} \leq \Lambda_3^{(1)}$, we must have $\Lambda_1^{(1)} < 0$ representing local compression and
 192 $\Lambda_3^{(1)} > 0$ representing local stretching (Ashurst *et al.* 1987), while the sign of intermediate
 193 eigenvalue is uncertain but has been found to most likely be positive in DNS of turbulent flows
 194 (Ashurst *et al.* 1987). The important point which can now be made on the basis of equation
 195 (2.12) is that uncertainty is always produced in the compressive direction ($\Lambda_1^{(1)} < 0$) and
 196 always attenuated in the stretching direction ($\Lambda_3^{(1)} > 0$). In the absence of external input of
 197 uncertainty, the growth of average uncertainty energy can only occur through compression
 198 events, and only if compression overwhelms stretching in $\langle P_{\Delta} \rangle$ and determines its sign.
 199 Spontaneous decorrelation of a flow from its perturbed flow in the absence of external inputs
 200 of uncertainty can only occur through local compressions.

201 3. Numerical setups

202 To study the growth of average uncertainty energy in periodic/homogeneous turbulence,
 203 we use a fully de-aliased pseudo-spectral code to perform DNS of forced incompressible
 204 Navier-Stokes turbulence in a periodic box of size $\mathcal{L}^3 = (2\pi)^3$. Time advancement is
 205 achieved with a second-order Runge-Kutta scheme. The code strategy is detailed by Vincent
 206 & Meneguzzi (1991). In all our simulations, the number of grid points is $N^3 = 512^3$ and
 207 the spatial resolution $\langle k_{max} \eta \rangle_t$ (see definition in caption of Table 1) is between 1.6 and
 208 1.7. The time step is calculated by the CFL condition and the CFL number is 0.4. We first
 209 generate a reference field and copy it but generate randomly the velocity field in the perturbed
 210 wavenumber range to create the perturbed flow at a time which we refer to as $t_0 = 0$, i.e.
 211 $\mathbf{u}^{(2)}(\mathbf{x}, t_0)$. In Fourier space, $\hat{\mathbf{u}}^{(2)}(\mathbf{k}, t_0)$ in each wavevector has six components:

$$212 \quad \hat{\mathbf{u}}^{(2)}(\mathbf{k}, t_0) = \begin{pmatrix} u_{x_0}^{(2)}(\mathbf{k}) e^{i\phi_{x_0}(\mathbf{k})} \\ u_{y_0}^{(2)}(\mathbf{k}) e^{i\phi_{y_0}(\mathbf{k})} \\ u_{z_0}^{(2)}(\mathbf{k}) e^{i\phi_{z_0}(\mathbf{k})} \end{pmatrix}, \quad (3.1)$$

213 which follow three constraints

214 (i) Incompressibility :

$$215 \quad i\mathbf{k} \cdot \hat{\mathbf{u}}^{(2)}(\mathbf{k}, t_0) = 0. \quad (3.2)$$

216 (ii) The initial energy spectra of the reference flow and the perturbed flow are identical:

$$217 \quad \hat{E}^{(1)}(k, t_0) = \int_{|\mathbf{k}|=k} \frac{|\hat{\mathbf{u}}^{(1)}(\mathbf{k}, t_0)|^2}{2} d^2\mathbf{k} = \int_{|\mathbf{k}|=k} \frac{|\hat{\mathbf{u}}^{(2)}(\mathbf{k}, t_0)|^2}{2} d^2\mathbf{k} = \hat{E}^{(2)}(k, t_0). \quad (3.3)$$

218 (iii) The difference initially only exists in the smallest scales, i.e. $|\mathbf{k}| > k_0$ where $k_0 =$
 219 $0.9k_{max}$ and $k_{max} = N/3$ is the maximum resolvable wavenumber after de-aliasing (see
 220 however Appendix A for different perturbed wavenumber ranges):

$$221 \quad \hat{\mathbf{u}}^{(2)}(\mathbf{k}, t_0) = \begin{cases} \hat{\mathbf{u}}^{(1)}(\mathbf{k}, t_0) & \text{if } |\mathbf{k}| < k_0, \\ \text{Randomly generated} & \text{if } |\mathbf{k}| \geq k_0. \end{cases} \quad (3.4)$$

222 For the generation of $\hat{\mathbf{u}}^{(2)}(\mathbf{k}, t_0)$ in the perturbed wavenumber range, these three constraints
 223 *a priori* couple all the $\hat{\mathbf{u}}^{(2)}(\mathbf{k}, t_0)$ on the sphere of Fourier space such that $|\mathbf{k}| = k$. For
 224 simplicity of implementation, we use a version of equation (3.3) restricted to each \mathbf{k} ,
 225 such that the sum of the resulting $\hat{\mathbf{u}}^{(2)}(\mathbf{k}, t_0)$ over $|\mathbf{k}| = k$ verifies equation (3.3). This
 226 means that for each wavevector \mathbf{k} we compute six random values, three moduli and three
 227 phases $\left[u_{x_0}^{(2)}(\mathbf{k}), u_{y_0}^{(2)}(\mathbf{k}), u_{z_0}^{(2)}(\mathbf{k}), \phi_{x_0}(\mathbf{k}), \phi_{y_0}(\mathbf{k}), \phi_{z_0}(\mathbf{k}) \right] \in [0, \sqrt{2\hat{E}^{(1)}}(k, t_0)]^3 \times [0, 2\pi]^3$
 228 that follow two constraints coming from the real and imaginary part of the incompressibility
 229 condition (equation (3.2)) and one constraint from the spectrum (equation (3.3)). This means
 230 that only three independent components have to be drawn and the three others will follow. In
 231 practice:

232 • In the general case of $k_x \neq 0$, $k_y \neq 0$ and $k_z \neq 0$, two uniform random numbers are
 233 drawn in $[0, 1)$ yielding $\phi_{x_0}(\mathbf{k})$ and $\phi_{y_0}(\mathbf{k})$ after rescaling and one uniform random number
 234 in $[0, 1)$ yielding $u_{z_0}^{(2)}(\mathbf{k})$ after rescaling. The moduli $u_{y_0}^{(2)}(\mathbf{k})$ and $u_{x_0}^{(2)}(\mathbf{k})$ are successively
 235 computed using equation (3.3). The sine and the cosine of the phase $\phi_{z_0}(\mathbf{k})$ are finally
 236 computed respectively using the real and imaginary part of the incompressibility condition
 237 (equation (3.2)).

238 • In the case where only one component of the wavevector is equal to zero: the modulus and
 239 the phase in the direction of the zero component of the wavevector are drawn first uniformly
 240 from $[0, \sqrt{2\hat{E}^{(1)}}(k, t_0)] \times [0, 2\pi)$. The two other moduli are computed using (equation (3.3)),
 241 one phase is drawn from $[0, 2\pi)$ and the other is deduced from incompressibility.

242 • In the case where two components of the wavevector are equal to zero: the real
 243 and imaginary parts of incompressibility impose that the modulus of the corresponding
 244 component of $\hat{\mathbf{u}}^{(2)}$ is zero, and that the corresponding phase is irrelevant. As a consequence,
 245 out of the four remaining values to be determined, one is constrained by equation (3.3). In
 246 practice the two remaining phases are drawn uniformly in $[0, 2\pi)^2$, one modulus is drawn
 247 uniformly in $[0, \sqrt{2\hat{E}^{(1)}}(k, t_0)]$ and the other is determined using (equation (3.3)).

248 In this way, the initial perturbations, defined as $\Delta\mathbf{u}(\mathbf{x}, t_0) = \mathbf{u}^{(2)}(\mathbf{x}, t_0) - \mathbf{u}^{(1)}(\mathbf{x}, t_0)$,
 249 are also incompressible and exist only in the perturbed wavenumber range. Furthermore, the
 250 perturbed flow is generated randomly in its perturbed wavenumber range, hence the reference
 251 flow and the perturbed flow are initially completely decorrelated in this wavenumber range,
 252 which implies.

$$253 \quad \hat{E}_\Delta(k, t_0) = \int_{|\mathbf{k}|=k} \frac{|\Delta\hat{\mathbf{u}}(\mathbf{k}, t_0)|^2}{2} d^2\mathbf{k} = \begin{cases} 0 & \text{if } |\mathbf{k}| < k_0, \\ \hat{E}_{\text{tot}}(k, t_0) & \text{if } |\mathbf{k}| \geq k_0, \end{cases} \quad (3.5)$$

254 where $\hat{E}_{\text{tot}}(k, t_0) = \hat{E}^{(1)}(k, t_0) + \hat{E}^{(2)}(k, t_0)$.

255 Three different cases (F1, F2 and F3) are simulated by applying different external forcings
 256 and initial conditions. In the first case, labelled F1, a negative damping forcing is applied to
 257 both the reference and the perturbed turbulent fields and the force-difference field does not
 258 vanish. The forcing function is divergence-free as it depends on the low wavenumber modes
 259 of the velocity in Fourier space as follows

$$260 \quad \hat{\mathbf{f}}^{(m)}(\mathbf{k}, t) = \begin{cases} \frac{\varepsilon_0}{2E_f^{(m)}} \hat{\mathbf{u}}^{(m)}(\mathbf{k}, t) & \text{if } 0 < |\mathbf{k}| \leq k_f, \\ 0 & \text{otherwise,} \end{cases} \quad (3.6)$$

261 where $\hat{\mathbf{f}}$ and $\hat{\mathbf{u}}$ are the Fourier transforms of \mathbf{f} and \mathbf{u} respectively, ε_0 is the preset average
 262 turbulence dissipation rate and E_f is the kinetic energy contained in the forcing bandwidth
 263 $0 < |\mathbf{k}| \leq k_f$. This forcing has been widely used to simulate statistically steady homogeneous
 264 isotropic turbulence (HIT) on the computer (Ho *et al.* 2020; Berera & Ho 2018; Boffetta

265 & Musacchio 2017; Mohan *et al.* 2017; Clark *et al.* 2022, 2021). It offers the advantage of
 266 setting the average turbulence dissipation a priori for statistically steady turbulence. In the
 267 present work, we set $\varepsilon_0 = 0.1$ and $k_f = 2.5$.

268 To generate the reference flow we use a von Kármán initial energy spectrum with the same
 269 coefficients as Yoffe (2012) and random initial Fourier phases. We integrate the reference
 270 flow till it reaches a statistically steady state and then seed it with perturbations to create the
 271 perturbed flow at a time which we refer to as $t_0 = 0$. One can see from equation (3.6) that
 272 the external forcings are determined separately by the two fields and therefore $\Delta \mathbf{f} \neq 0$. F1
 273 is the only one of our three cases where F_Δ is not identically zero and some uncertainty is
 274 introduced by the forcing in equation (2.4).

275 The case F2 is identical to F1 except for the external forcing which is such that $F_\Delta = 0$.
 276 The forcing in the perturbed field is determined by the velocity in the reference field as

$$277 \quad \hat{\mathbf{f}}^{(2)}(\mathbf{k}, t) = \hat{\mathbf{f}}^{(1)}(\mathbf{k}, t) = \begin{cases} \frac{\varepsilon_0}{2E_f^{(1)}} \hat{\mathbf{u}}^{(1)}(\mathbf{k}, t) & \text{if } 0 < |\mathbf{k}| \leq k_f, \\ 0 & \text{otherwise,} \end{cases} \quad (3.7)$$

278 where $\varepsilon_0 = 0.1$ and $k_f = 2.5$. Therefore, there is no forcing difference between the two fields
 279 and all the uncertainty in equation (2.4) is generated exclusively by the internal production.

280 The case F3 differs in one essential way from F1 and F2: rather than force the turbulence
 281 into a stationary steady state and then introduce the uncertainty after stationarity has set
 282 in (as in F1 and F2), in F3 we introduce the uncertainty well before stationarity has set
 283 in, i.e. at a very initial time when the initial velocity field has very little energy and the
 284 simulation starts running with a forcing which eventually brings the turbulence into an
 285 energetic stationary state. We chose a forcing for F3 that is independent of the velocity field
 286 to ensure steady buildup of the turbulence during a long yet finite time. The initial velocity
 287 fields are randomly generated with the same energy spectrum $\hat{E}(k) = 0.3 \times 10^{-4} k^{-1}$ for
 288 the reference and the perturbed fields and the initial perturbations are seeded in the high
 289 wavenumber Fourier phases in the exact same way as in F1 and F2. Both flows are forced by
 290 an identical single-mode divergence-free force

$$291 \quad \mathbf{f}^{(2)}(\mathbf{x}, t) = \mathbf{f}^{(1)}(\mathbf{x}, t) = \begin{pmatrix} \cos(k_0 y) \sin(k_0 z) \\ \cos(k_0 z) \sin(k_0 x) \\ \cos(k_0 x) \sin(k_0 y) \end{pmatrix}, \quad (3.8)$$

292 where $k_0 = 4$. This forcing differs from F1 but is similar to F2 in that F_Δ identically vanishes
 293 and there is no uncertainty input from the forcing in equation (2.4). We repeat, however,
 294 that the main distinguishing feature of F3 compared to F1 and F2 is that, in F3, the reference
 295 and the perturbed fields are statistically non-stationary during their initial growth (driven by
 296 the forcing) and the concurrent initial growth of uncertainty. This non-stationarity affects
 297 equation (2.4) through the resulting non-stationarity of the strain rate field in the internal
 298 production rate.

299 In summary, F1 is the case that is widely used in previous works (Ho *et al.* 2020; Berera
 300 & Ho 2018; Boffetta & Musacchio 2017; Mohan *et al.* 2017; Clark *et al.* 2022, 2021) and F2
 301 differs from it only in terms of $\Delta \mathbf{f}$ which is zero in F2 and non-zero in F1. In both F1 and
 302 F2 the perturbation is made to a fully developed statistically stationary turbulence whereas
 303 in F3 we follow the evolution of two velocity fields which are initially very weak in terms of
 304 energy and very close to each other, i.e. very highly correlated. Both flows are progressively
 305 intensified by the same spatially sinusoidal time-independent forcing field and evolve towards
 306 statistical stationary fully developed turbulence while, at the same time, diverging from each
 307 other.

308 The main parameters characterising the reference flows are given in table 1 where $\langle \cdot \rangle$

Case	N^3	ν	$\langle\langle\varepsilon\rangle\rangle_t$	$\langle U \rangle_t$	$\langle L \rangle_t$	$\langle T_0 \rangle_t$	$\langle \text{Re} \rangle_t$	$\langle \text{Re}_\lambda \rangle_t$	$\langle k_{\max} \eta \rangle_t$
F1	512^3	0.0010	0.0981	0.622	1.101	1.771	684.9	151.6	1.70
F2	512^3	0.0010	0.0988	0.622	1.102	1.772	685.4	151.2	1.70
F3	512^3	0.0015	0.4096	0.643	0.345	0.537	148.2	63.8	1.62

Table 1: Parameters of the reference flows, where $\langle \cdot \rangle$ represents the spatial average; $\langle \cdot \rangle_t$ represents the temporal average and $\langle\langle \cdot \rangle\rangle_t$ represents the average in both space and time. N is the resolution of the simulations, ν is the kinematic viscosity, ε is the dissipation.

$U \equiv \sqrt{2 \langle E \rangle / 3}$ is the rms velocity and $L \equiv (3\pi/4 \langle E \rangle) \int k^{-1} \hat{E}(k) dk$ is the integral length scale. $T_0 \equiv L/U$ is the large eddy turnover time. $\text{Re} \equiv UL/\nu$ is the Reynolds number. $\text{Re}_\lambda \equiv Ul_\lambda/\nu$ is the Reynolds number defined by the Taylor length scale $l_\lambda \equiv \sqrt{10 \langle E \rangle \nu / \langle \varepsilon \rangle}$. k_{\max} is the maximum resolvable wavenumber and $\eta \equiv (\nu^3 / \langle \varepsilon \rangle)^{1/4}$ is the Kolmogorov scale.

309 represents the spatial average, $\langle \cdot \rangle_t$ represents the temporal average and $\langle\langle \cdot \rangle\rangle_t$ represents the
310 average in both space and time. For F1 and F2, this time average is over all time $t \geq 0$
311 when the reference and perturbed fields are statistically stationary in the simulations. For
312 F3, the time average is over the time when the reference flow's turbulent kinetic energy
313 and dissipation rate are statistically stationary, i.e. the standard deviations of $\langle E^{(1)} \rangle(t)$
314 and $\langle \varepsilon^{(1)} \rangle(t)$ are smaller than 8% of $\langle\langle E^{(1)} \rangle\rangle_t$ and $\langle\langle \varepsilon^{(1)} \rangle\rangle_t$ respectively. This leads to
315 $\tau \equiv t / \langle T_0^{(1)} \rangle_t \in [9.4, 30.0]$ (Note that the dimensionless time $\tau \equiv t / \langle T_0^{(1)} \rangle_t$ is defined for
316 all three cases F1, F2 and F3.).

317 4. DNS results

318 In this section we present our DNS results concerning equation (2.4), starting in subsection
319 4.1 with the time evolution of $\langle E_\Delta \rangle$ during the decorrelation process and an analysis of the
320 three mechanisms at play and of the uncertainty's energy spectrum. In subsection 4.2 we
321 relate the growth rate of $\langle E_\Delta \rangle$ to detailed properties of the production and dissipation of
322 uncertainty, of the strain rate eigenvalues and of the distribution of uncertainty energy in the
323 three principal axes of the strain rate tensor. In particular, we derive the chaotic exponential
324 growth of $\langle E_\Delta \rangle$ from similarity behaviours of these quantities. In subsection 4.3 we go beyond
325 the average production of uncertainty and report probability density functions of P_Δ .

326 4.1. Time evolution of uncertainty

327 4.1.1. Uncertainty energy

328 Figure 1 shows the time evolutions of $\langle E_\Delta \rangle$ for each case F1, F2 and F3. The very first thing
329 that happens immediately after the perturbations are seeded is a decrease of $\langle E_\Delta \rangle$ in all three
330 cases. This initial correlating action is caused by the concentration of the initial perturbations
331 at the highest wavenumbers where dissipation is high. The insets of figure 2 show that $\langle \varepsilon_\Delta \rangle$ is
332 orders of magnitude higher than $\langle P_\Delta \rangle$ at the earliest times in all three cases. As time proceeds,
333 the uncertainty's dissipation rate decreases and its production rate increases till production
334 overtakes dissipation (see figure 2) and $\langle E_\Delta \rangle$ begins to grow. This initial growth is shown in
335 the insets of figure 1 and it differs for F1 and F2 on the one hand and F3 on the other. For F1
336 and F2, $\langle E_\Delta \rangle$ is observed to grow exponentially in the approximate time-range $\tau \in [0.2, 2.9]$.
337 Previous DNS studies have already observed such exponential growth (Berera & Ho 2018;

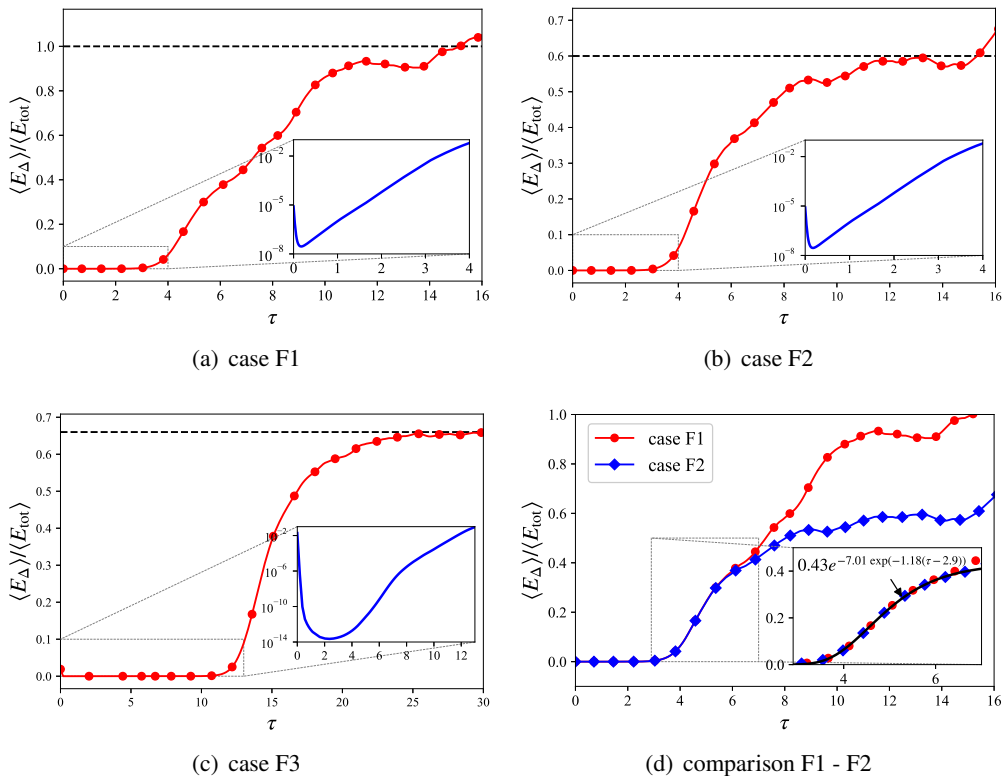


Figure 1: Time evolutions of average uncertainty energy for different cases. Inset: the initial time evolution of average uncertainty energy in semilogarithmic plot. The uncertainty evolutions of F1 and F2 are presented together in (d). Inset: the uncertainty evolutions during $\tau \in [2.9, 6.5]$. The exponential of exponential function fit is indicated by a solid black line.

338 Boffetta & Musacchio 2017). For F3, the initial growth is from $\tau \approx 2.5$ to $\tau \approx 12.6$ and is
 339 subdivided in two parts. In the time range $\tau \in [2.5, 7.5]$, the turbulence and its strain rate
 340 are not statistically stationary and the time evolution of $\langle E_{\Delta} \rangle$ is not exponential. Indeed, the
 341 plot of the logarithm of $\langle E_{\Delta} \rangle$ versus time in the inset of figure 1(c) has a positive curvature
 342 in that time range. An exponential growth of $\langle E_{\Delta} \rangle$ appears to set in at $\tau \approx 7.5$ and lasts till
 343 about $\tau \approx 12.6$. It is noteworthy that an exponential growth of uncertainty also exists in F3
 344 and that it starts a little earlier than when stationarity sets in. (The exponential regime's time
 345 range is longer for F3 than for F1 and F2 mainly because of F3's lower Reynolds number as
 346 argued in Appendix B). The results and analysis in the remainder of this paper confirm these
 347 interpretations.

348 The growths of $\langle E_{\Delta} \rangle$ are identical in F1 and F2 (see figure 1(d)) till the time when $\langle F_{\Delta} \rangle$
 349 becomes significantly non-zero in F1 (see figure 2(a)). The regime of exponential growth
 350 is followed by what appears to be an exponential of exponential regime from $\tau \approx 2.9$ to
 351 $\tau \approx 6.5$. This exponential of exponential growth is the same in F1 and F2 and is highlighted
 352 by the fit in the inset of figure 1(d). A similar growth range has been observed in previous
 353 DNS that are similar to F1 and go up to even higher Reynolds numbers (Berera & Ho 2018;
 354 Boffetta & Musacchio 2017). This exponential of exponential growth is confirmed by our
 355 analysis and further DNS results in subsection 4.2.

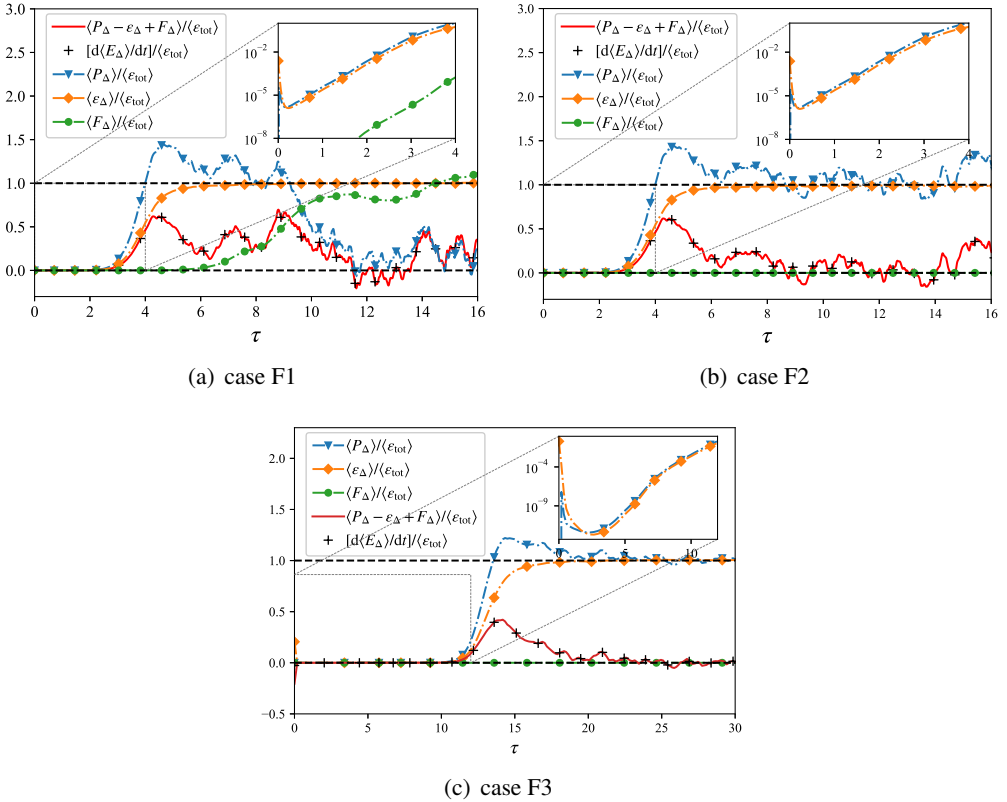


Figure 2: Time evolutions of each term in equation (2.4) for different cases, where $\varepsilon_{\text{tot}} = \varepsilon^{(1)} + \varepsilon^{(2)}$ is the total dissipation of the reference and perturbed fields. Inset: the initial time evolution of the internal production, dissipation and external input/output in semilogarithmic plot.

356 After time $\tau = 6.5$, the uncertainty grows for F1 and F2 deviate from each other as shown
 357 in figure 1(d) ($\frac{|\langle E_{\Delta} \rangle_{F1} - \langle E_{\Delta} \rangle_{F2}|}{\langle E_{\Delta} \rangle_{F1}} > 5\%$) and growing as τ grows above 6.5) because $\langle F_{\Delta} \rangle$ starts
 358 growing significantly above zero ($\langle F_{\Delta} \rangle / \langle \varepsilon_{\Delta} \rangle = 0.06$ at $\tau = 6.5$) in F1 whereas it is identically
 359 zero in F2 for all time (see figure 2). The reference and perturbed fields achieve significant
 360 decorrelation after the exponential growth of $\langle E_{\Delta} \rangle$ for both F1 and F2, resulting, in case F1,
 361 in non-zero values of $\langle F_{\Delta} \rangle$ which eventually grow significantly above the reference field's
 362 turbulence dissipation rate, but only after $\tau = 6.5$. The additional external decorrelating
 363 action of the forcing leads to eventually fully decorrelated reference and perturbed fields in
 364 case F1 as the ratio $\langle E_{\Delta} \rangle / \langle E_{\text{tot}} \rangle$ stops growing and saturates at 0.97 ± 0.07 after $\tau = 10.6$. In
 365 case F2 the identical forcing in both fields acts as a perpetual partially correlating (rather than
 366 decorrelating) action of the two fields and to a resulting eventual saturation of $\langle E_{\Delta} \rangle / \langle E_{\text{tot}} \rangle$
 367 at 0.59 ± 0.05 for $\tau \geq 8.9$ (In Appendix A we provide evidence showing that the early- and
 368 mid-time evolutions (i.e. the exponential regime and the exponential of exponential regime)
 369 of the average uncertainty energy are not very sensitive to the form and amplitude of the
 370 initial perturbations.).

371 For case F3, the growth of $\langle E_{\Delta} \rangle$ following the exponential regime ending at about $\tau \approx 12.6$
 372 can be seen in figure 1(c) and cannot be fitted by the exponential of exponential function
 373 detected in cases F1 and F2 nor any clear linear or power-law growth functions. As in F2,

Case	Uncertainty regime	Time interval τ
F1	Initial decrease	[0, 0.2]
	Exponential growth	[0.2, 2.9]
	Exponential of exponential growth	[2.9, 6.5]
	Linear growth	[6.5, 10.6]
	Saturation	[10.6, $+\infty$]
F2	Initial decrease	[0, 0.2]
	Exponential growth	[0.2, 2.9]
	Exponential of exponential growth	[2.9, 6.5]
	Transient growth	[6.5, 8.9]
	Saturation	[8.9, $+\infty$]
F3	Initial decrease	[0, 2.5]
	Unsteady initial growth	[2.5, 7.5]
	Exponential growth	[7.5, 12.6]
	Nonlinear growth	[12.6, 25.3]
	Saturation	[25.3, $+\infty$]

Table 2: Time ranges of different uncertainty growth regimes.

374 the correlating action of the identical external forcing in both the reference and perturbed
375 fields leads to them remaining partially correlated at all times and to an eventual saturation
376 of $\langle E_\Delta \rangle / \langle E_{\text{tot}} \rangle$ at 0.66 ± 0.01 for $\tau \geq 25.3$.

377 We close this subsection by pointing out that the only case of linear growth that we may
378 have detected in our DNS is for F1 in the time range $\tau \in [6.5, 10.6]$. A linear growth regime
379 has been predicted by Aurell *et al.* (1997), however our simulations suggest that it may
380 depend on the type of forcing. Furthermore, the Reynolds number of our DNS may not be
381 high enough to observe it clearly and the very level of Reynolds number required may itself
382 depend on the external forcing. We examine this issue again in the following subsections.
383 The time ranges of the different uncertainty growth regimes in each case F1, F2 and F3 are
384 summarized in table 2.

385 4.1.2. Mechanisms of the uncertainty evolution

386 The time evolutions of each term in equation (2.4), including the growth rate $d\langle E_\Delta \rangle / dt$
387 obtained directly from the DNS, are shown in figure 2. As can be seen in the figure, we
388 started by checking that $d\langle E_\Delta \rangle / dt$ agrees well with its value obtained from equation (2.4).
389 In all cases F1, F2 and F3, $\langle P_\Delta \rangle > \langle \varepsilon_\Delta \rangle$ when $d\langle E_\Delta \rangle / dt > 0$. In cases F2 and F3 where
390 $\langle F_\Delta \rangle = 0$ at all times, the eventual saturation when $d\langle E_\Delta \rangle / dt \approx 0$ is characterised by
391 the balance $\langle P_\Delta \rangle \approx \langle \varepsilon_\Delta \rangle$. This balance reflects the long-time partial correlation between the
392 reference and perturbed fields and the long-time saturation of $\langle E_\Delta \rangle / \langle E_{\text{tot}} \rangle$ at a value smaller
393 than 1 reported in the previous subsection.

394 We also observe in figure 2 for all cases F1, F2 and F3 that the long-time saturation is
395 such that $\langle \varepsilon_\Delta \rangle \approx \langle \varepsilon_{\text{tot}} \rangle \equiv \langle \varepsilon^{(1)} + \varepsilon^{(2)} \rangle$ which implies $\langle \varepsilon_{\text{corr}} \rangle \approx 0$. In cases F2 and F3,
396 this means that the long-time saturated non-zero steady state of $\langle P_\Delta \rangle$ is such that $\langle P_\Delta \rangle \approx$
397 $\langle \varepsilon^{(1)} + \varepsilon^{(2)} \rangle \approx \langle F^{(1)} + F^{(2)} \rangle$ (recall $\langle F_\Delta \rangle = 0$ and $\langle F_{\text{corr}} \rangle = 0$ in F2, F3): the correlating
398 action by the identical forcing in both statistically stationary reference and perturbed fields
399 is directly balanced by the decorrelating action of the internal production of uncertainty.

400 The uncertainty dissipation rate $\langle \varepsilon_\Delta \rangle$ reaches its long-time asymptotic balance with $\langle \varepsilon_{\text{tot}} \rangle$,
401 i.e. $\langle \varepsilon_\Delta \rangle / \langle \varepsilon_{\text{tot}} \rangle > 0.95$, at about $\tau = 16.1$ for F3 and at about $\tau = 5.6$ for both F1 and F2.
402 This is slightly before but close to the time $\tau = 6.5$ when $\langle F_\Delta \rangle / \langle \varepsilon_\Delta \rangle = 0.06$ stops being

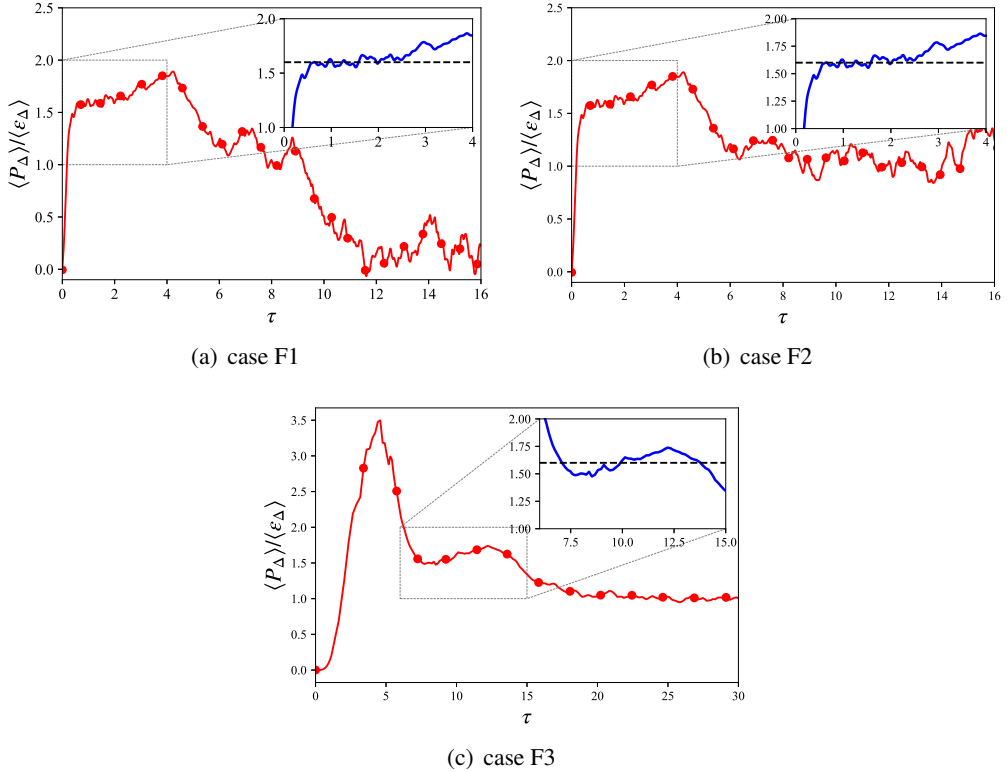


Figure 3: Time evolutions of ratio $\langle P_\Delta \rangle / \langle \varepsilon_\Delta \rangle$ for different cases. Inset: the evolution of the ratio in the time range of the exponential growth of the average uncertainty.

403 negligible in F1 and the perturbation evolutions start diverging between F1 and F2. The
 404 presence of positive $\langle F_\Delta \rangle$ in F1 delays the decay towards 0 of $d\langle E_\Delta \rangle / dt$ which is reached
 405 at about $\tau = 10.6$ for F1 but $\tau = 8.9$ for F2. In the case of F1 one might even argue that
 406 an approximate steady state has resulted for $d\langle E_\Delta \rangle / dt$ between $\tau = 6.5$ and $\tau = 10.6$, the
 407 time range corresponding to the linear growth regime perhaps observed in figure 1(a) for
 408 F1 and also in some previous DNS (Berera & Ho 2018; Boffetta & Musacchio 2017). After
 409 $\tau = 10.6$, $\langle P_\Delta \rangle$ oscillates around zero, corresponding to the saturation of $\langle E_\Delta \rangle / \langle E_{\text{tot}} \rangle$ at a
 410 value 0.97 ± 0.07 in figure 1(a). This reflects the total decorrelation between the F1 reference
 411 and perturbed fields and leads to a long-time saturation balance $\langle F_\Delta \rangle \approx \langle \varepsilon_\Delta \rangle$ in F1 which is
 412 to be contrasted with $\langle P_\Delta \rangle \approx \langle \varepsilon_\Delta \rangle$ in F2 and F3. Note that the long-time saturation is such
 413 that $\langle F_{\text{corr}} \rangle \approx 0$ and $\langle F_\Delta \rangle \approx \langle F^{(1)} + F^{(2)} \rangle$ in all cases, including F1. Hence, the long-time
 414 saturation balance between $\langle F_\Delta \rangle$ and $\langle \varepsilon_\Delta \rangle$ in case F1 simply reflects $\langle \varepsilon_{\text{tot}} \rangle \approx \langle F^{(1)} + F^{(2)} \rangle$.
 415 In figure 3 we concentrate on the time-evolution of the production-dissipation ratio
 416 $\langle P_\Delta \rangle / \langle \varepsilon_\Delta \rangle$ in all three cases F1, F2 and F3. As highlighted in the insets of this figure's plots,
 417 there is, in all three cases, a time range when $\langle P_\Delta \rangle / \langle \varepsilon_\Delta \rangle$ is about constant, i.e. a time range
 418 when the evolutions of $\langle P_\Delta \rangle$ and $\langle \varepsilon_\Delta \rangle$ are similar. In all three cases this time range includes
 419 the time range of exponential growth of $\langle E_\Delta \rangle$ identified in the previous subsection; in fact,
 420 in case F3 it more or less exactly coincides with it. To be specific, $\langle P_\Delta \rangle / \langle \varepsilon_\Delta \rangle = 1.61 \pm 0.03$
 421 from $\tau = 0.6$ to $\tau = 2.5$ for F1 and F2, and $\langle P_\Delta \rangle / \langle \varepsilon_\Delta \rangle = 1.61 \pm 0.08$ from $\tau = 7.2$ to $\tau = 12.8$
 422 for F3. These two values are very close (and the additional case F4 in Appendix B returns a
 423 similar value for $\langle P_\Delta \rangle / \langle \varepsilon_\Delta \rangle$ in F4's similarity regime), indicating that the similarity value of

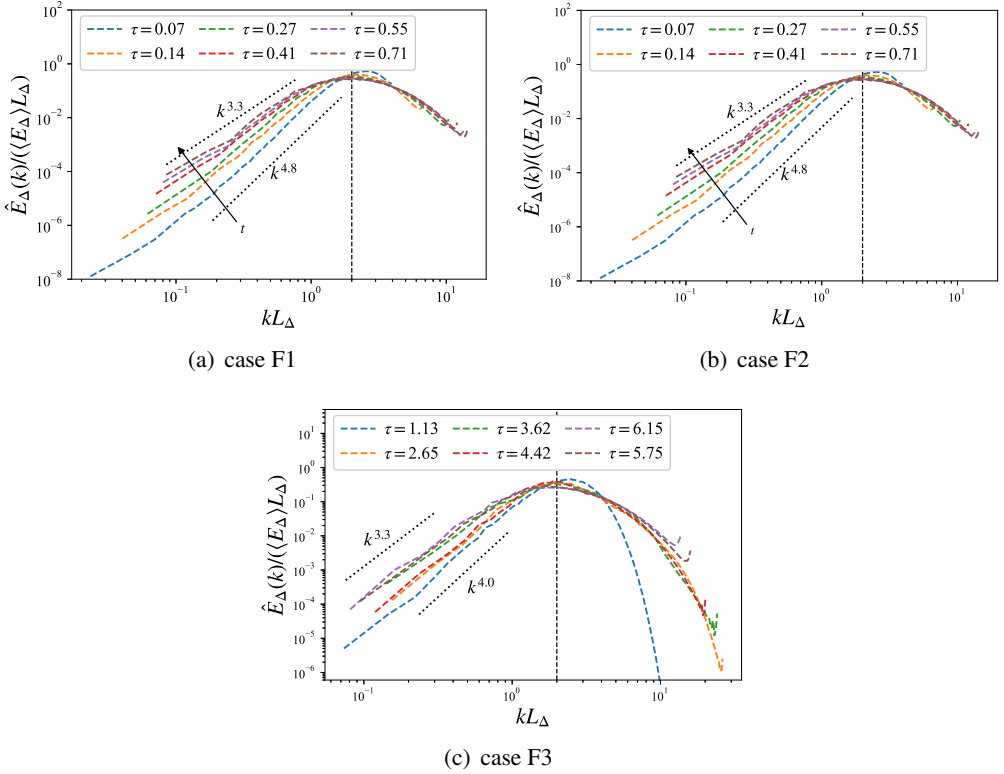


Figure 4: Early-time evolution of uncertainty energy spectrum for different cases. The spectra are normalized by $\langle E_\Delta \rangle$ and L_Δ .

424 the production-dissipation ratio $\langle P_\Delta \rangle / \langle \varepsilon_\Delta \rangle$ might be universal and independent of Reynolds
 425 number, as the presence of a strange attractor might perhaps imply.

426 4.1.3. Uncertainty spectrum

427 The uncertainty dissipation rate is the integral over all wavenumbers k of $k^2 \hat{E}_\Delta(k)$ where
 428 $\hat{E}_\Delta(k)$ is the uncertainty spectrum, i.e. the energy spectrum of the velocity difference field.
 429 The similarity in the evolutions of uncertainty production and dissipation rates raises the
 430 question whether the uncertainty spectrum evolves in some self-similar manner over the
 431 time range of that similarity. We answer this question in terms of the integral length scale
 432 of the velocity-difference fields considered here which is $L_\Delta = (3\pi/4 \langle E_\Delta \rangle) \int k^{-1} \hat{E}_\Delta(k) dk$
 433 (see Batchelor (1953) for an introduction to this length scale for any statistically homoge-
 434 neous/periodic velocity field). L_Δ is a measure of the length over which the velocity difference
 435 field is correlated, i.e. a characteristic length scale of uncertainty containing eddies.

436 Soon after the initial decay of $\langle E_\Delta \rangle$, the uncertainty spectra collapse with $\langle E_\Delta \rangle(t)$ and
 437 $L_\Delta(t)$ at wavenumbers larger than $2/L_\Delta$ as shown in figure 4, i.e. $\hat{E}_\Delta(k, t) = \langle E_\Delta \rangle L_\Delta f(kL_\Delta)$
 438 for $kL_\Delta \geq 2$, where f is a dimensionless function of dimensionless wavenumber. At
 439 wavenumbers $kL_\Delta < 1$ the energy spectra have an approximately power law dependence
 440 on k but do not collapse till soon after the time when the exponential growth of $\langle E_\Delta \rangle(t)$ and
 441 the uncertainty's production-dissipation similarity ($\langle P_\Delta \rangle / \langle \varepsilon_\Delta \rangle \approx 1.6 - 1.7$) sets in. Over the
 442 time range when $\langle P_\Delta \rangle / \langle \varepsilon_\Delta \rangle \approx 1.6 - 1.7$, the uncertainty spectrum is self-similar, i.e. evolves
 443 as $\hat{E}_\Delta(k, t) = \langle E_\Delta \rangle L_\Delta f(kL_\Delta)$ for all wavenumbers (see figure 5). The peak of the spectrum

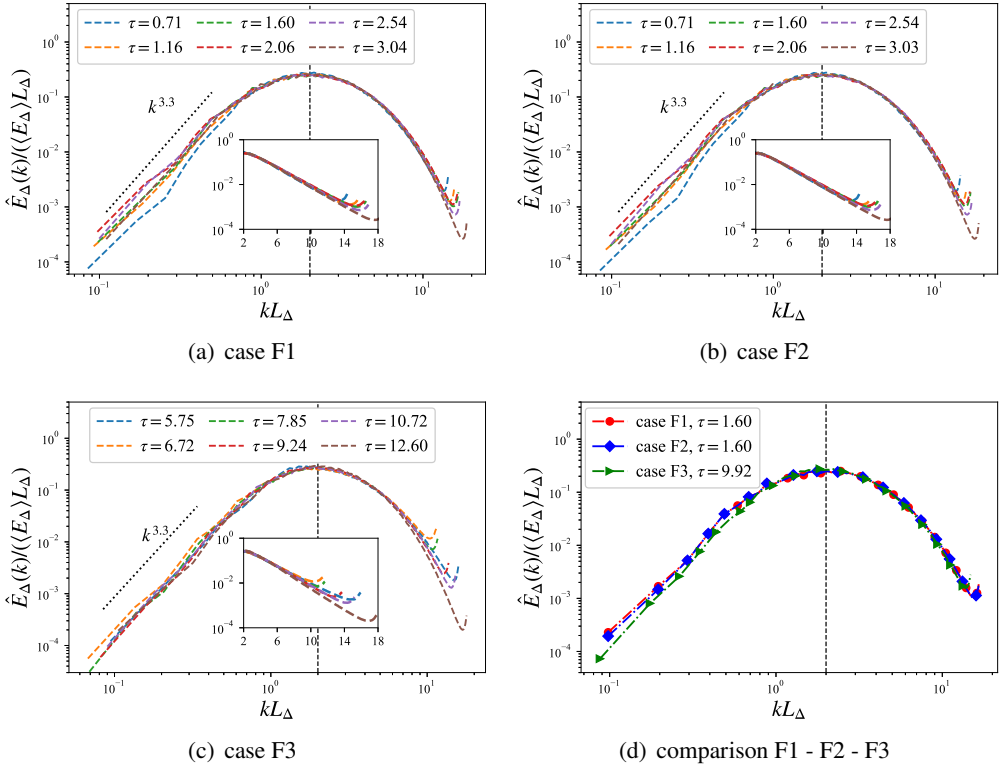


Figure 5: Uncertainty energy spectra for cases (a) F1, (b) F2 and (c) F3 in the similarity regime. The spectra are normalized by $\langle E_\Delta \rangle$ and L_Δ . Inset: semilogarithmic plot of the uncertainty spectra in the wavenumber range higher than $2/L_\Delta$. The collapse of the normalized uncertainty spectra for cases F1, F2 and F3 in the similarity regime is shown in (d).

444 is at $k \approx 2/L_\Delta$ in all three cases F1, F2 and F3. At wavenumbers below $2/L_\Delta$ the uncertainty
 445 spectra have an approximately $k^{3.3}$ power law shape, while at wavenumbers above $2/L_\Delta$,
 446 they appear to have an exponential shape. Similar uncertainty spectrum shapes have been
 447 found in a previous DNS study (Berera & Ho 2018).

448 It is remarkable that the uncertainty spectrum is self-similar in case F3 in the exact same
 449 way that it is self-similar in cases F1 and F2 over the time range where $\langle P_\Delta \rangle / \langle \varepsilon_\Delta \rangle$ is
 450 approximately constant. In fact, the self-similar uncertainty spectrum even seems to be
 451 the same for F3, F1 and F2 as seen by the collapse in figure 5(d), suggesting a universal shape
 452 for the self-similar uncertainty spectrum in HIT. This is remarkable not only because F3 has
 453 a very different Reynolds number and forcing than F1 and F2, but more importantly because
 454 the F3 reference field is not statistically stationary in that time range whereas the F1 and F2
 455 reference fields are. In the F3 case, the uncertainty spectrum reaches its self-similar state at
 456 $\tau \approx 5.8$ and the reference field becomes statistically stationary at $\tau = 9.4$.

457 After the time-range where $\langle P_\Delta \rangle / \langle \varepsilon_\Delta \rangle$ is approximately constant, the uncertainty spectrum
 458 is no longer self-similar (see figure 6). This happens at $\tau = 3.5$ for cases F1 and F2 and
 459 at $\tau = 12.6$ for case F3 when $\hat{E}_\Delta(k_{max})/\hat{E}_{tot}(k_{max}) > 0.95$. These are the times when the
 460 reference and perturbed fields decorrelate at the largest resolvable wavenumber (see figure
 461 6). The process of decorrelation between the two fields proceeds by decorrelating them at
 462 progressively smaller wavenumbers, causing the uncertainty spectrum to collapse with the

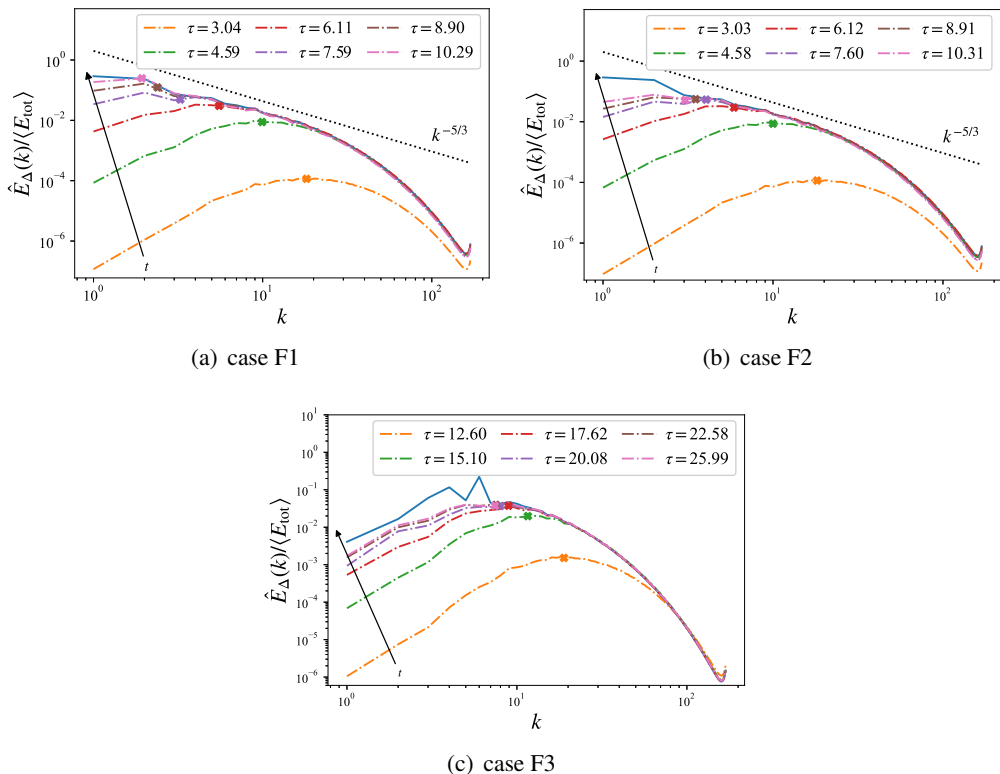


Figure 6: Uncertainty spectra (dash lines) for different cases after the times when the reference and perturbed fields decorrelate at the largest resolvable wavenumber. The uncertainty spectra are normalized by $\langle E_{\text{tot}} \rangle$. The dots on the uncertainty spectra represent $k = 2/L_\Delta$. The solid line represents the energy spectrum of the reference field when it is statistically steady. The energy spectrum is normalized by $\langle E^{(1)} \rangle$. The uncertainty spectrum shifts gradually along with the arrows representing the direction of time advance.

463 reference field's energy spectrum over a progressively wider range of the higher wavenumbers
 464 (see figure 6). This progressive decorrelation process from high to small wavenumbers and
 465 the uncertainty spectrum's progressive convergence towards the reference field's spectrum
 466 prevents the uncertainty spectrum from being self-similar. For F1, the uncertainty spectrum
 467 finally collapses with the reference field's energy spectrum at all wavenumbers, indicating
 468 that the two fields eventually decorrelate completely at all wavenumbers (see figure 6(a)).
 469 The same happens for F2 and F3 except over the wavenumbers acted by the forcing where a
 470 gap always remains between the uncertainty and the reference field spectra, indicating that
 471 the two fields retain a degree of correlation at these large scales (see figure 6(b), 6(c)).

472 4.1.4. Characteristic length of uncertainty

473 The growth of L_Δ is evident in figure 6. We therefore plot its time evolution in figure 7 and
 474 compare it with the integral and Taylor length scales (L and l_λ respectively) of the reference
 475 field for each case F1, F2 and F3. At the very early times when uncertainty dissipation
 476 dominates, the velocity-difference field decays and its integral length scale normalised by
 477 L is, correspondingly, increasing. In the stationary turbulence F1 and F2 cases, this time
 478 regime is followed by the chaotic regime where $\langle E_\Delta \rangle$ grows exponentially and where $L_\Delta/l_\lambda^{(1)}$

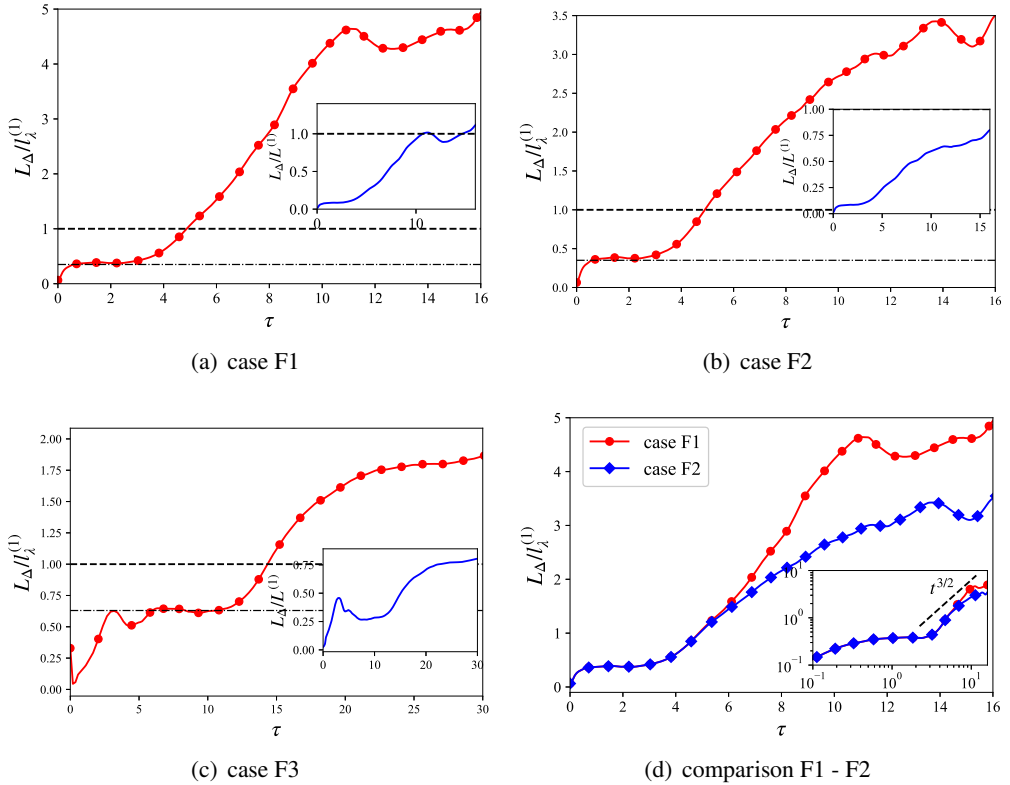


Figure 7: Time evolution of $L_{\Delta}/l_{\lambda}^{(1)}$ for different cases. Inset: time evolution of $L_{\Delta}/L^{(1)}$.

The time evolutions of $L_{\Delta}/l_{\lambda}^{(1)}$ in cases F1 and F2 are plotted together in (d). Inset: the log-log plot of the time evolutions of $L_{\Delta}/l_{\lambda}^{(1)}$.

479 remains relatively constant at 0.38 ± 0.01 . A constant $L_{\Delta}/l_{\lambda}^{(1)}$ (though a different constant,
 480 $L_{\Delta}/l_{\lambda}^{(1)} = 0.64 \pm 0.03$) is also observed in the non-stationary F3 case during the chaotic
 481 regime even though $l_{\lambda}^{(1)}$ grows in time for some of that regime and even though this time
 482 regime does not follow immediately after the dissipation-dominated regime. In fact, L_{Δ}
 483 decreases between the dissipation-dominated and the chaotic regime in the F3 case. It is
 484 noteworthy that L_{Δ} reaches $l_{\lambda}^{(1)}$ at $\tau = 4.9$ for cases F1 and F2 and at $\tau = 14.5$ for case F3,
 485 a little before the average uncertainty dissipation rate reaches its stationary value in figure
 486 2, i.e. $\tau \approx 5.6$ for F1 and F2 and $\tau \approx 16.1$ for F3. The link between L_{Δ} and the Taylor
 487 length of the reference field is potentially interesting as the Taylor length is the mean distance
 488 between stagnation points in a homogeneous isotropic turbulence (Goto & Vassilicos 2009)
 489 and therefore tends to represent the average size of turbulent eddies which is highly weighted
 490 towards the more numerous smallest ones.

491 Following the exponential growth of $\langle E_{\Delta} \rangle$, three consecutive time regimes follow for F1
 492 and F2. First, one observes an approximately power-law growth of L_{Δ} , identical for both F1
 493 and F2 as shown in figure 7(d), more or less coinciding with the exponential of exponential
 494 growth of $\langle E_{\Delta} \rangle$ till $\tau = 6.5$. In this time regime, $L_{\Delta} \sim t^{3/2}$ is a good fit. This fit is reminiscent
 495 of the power-law growth of the predictability scale $k_E^{-1} \sim t^{3/2}$ obtained in previous numerical
 496 simulations (Boffetta & Musacchio 2017; Leith & Kraichnan 1972) and theoretical arguments

497 (Boffetta & Musacchio 2017; Lorenz 1969; Frisch 1995), as a companion conclusion to the
 498 linear growth of $\langle E_\Delta \rangle$. However, L_Δ and k_E^{-1} are not equivalent: the predictability scale is
 499 defined as the inverse of the minimum wavenumber k_E such that $\hat{E}_\Delta(k_E)/\hat{E}_{\text{tot}}(k_E) = 1$,
 500 and $k_E^{-1} \sim t^{3/2}$ is obtained on the assumption that the decorrelation process happens in
 501 the inertial range. $L_\Delta \sim t^{3/2}$ is observed without concurrent linear growth of $\langle E_\Delta \rangle$ but a
 502 concurrent exponential or exponential $\langle E_\Delta \rangle$ growth instead.

503 The second consecutive regime which follows for F1 and F2 is an apparently linear growth
 504 of L_Δ that lasts till the time when L_Δ saturates to a constant. The third and final regime is this
 505 approximately constant L_Δ regime where $L_\Delta \approx L^{(1)}$ for F1 (see figure 7(a)) in agreement
 506 with the eventual complete decorrelation of the reference and perturbed fields and where
 507 $L_\Delta \approx (0.70 \pm 0.06)L^{(1)}$ (smaller than $L^{(1)}$) for F2 (see figure 7(b)) in agreement with the
 508 eventual partial correlation between these two fields in this case.

509 In the F3 case, the chaotic regime where $\langle E_\Delta \rangle$ grows exponentially and $L_\Delta/l_\lambda^{(1)} = 0.64 \pm$
 510 0.03 is followed by an intermediate regime where L_Δ grows to eventually reach the final
 511 constant regime where $L_\Delta = (0.81 \pm 0.03)L^{(1)}$ (smaller than $L^{(1)}$) characterising the final
 512 saturation (see figure 7(c)). As for F2, the fact that L_Δ is significantly lower than L in the
 513 eventual saturation regime reflects the partial long-time correlation imposed by the identical
 514 forcing in the reference and perturbed fields.

515 4.2. Quantitative analysis of the uncertainty growth

516 4.2.1. From similarity to exponential growth

517 When $\langle F_\Delta \rangle$ is identically zero (as in F2 and F3) or negligibly small compared to $\langle P_\Delta \rangle$ and
 518 $\langle \varepsilon_\Delta \rangle$ (as in F1 for τ smaller than about 6.5) the evolution equation for $\langle E_\Delta \rangle$ becomes

$$519 \quad \frac{d}{dt} \langle E_\Delta \rangle = \langle P_\Delta \rangle - \langle \varepsilon_\Delta \rangle. \quad (4.1)$$

520 To estimate $\langle P_\Delta \rangle$ in terms of $\langle E_\Delta \rangle$ and obtain an equation of the same form as equation (1.1),
 521 we apply a Reynolds decomposition to equation (2.12) and write

$$522 \quad \langle P_\Delta \rangle = - \sum_{i=1}^3 \left\langle \Lambda_i^{(1)} \Delta w_i^2 \right\rangle = - \underbrace{\sum_{i=1}^3 \left\langle \Lambda_i^{(1)} \right\rangle \langle \Delta w_i^2 \rangle}_{\langle P_\Delta \rangle_{\text{Ave}}} - \underbrace{\sum_{i=1}^3 \left\langle \Lambda_i^{(1)'} \Delta w_i^{2'} \right\rangle}_{\langle P_\Delta \rangle_{\text{Fluc}}}, \quad (4.2)$$

523 where $\Lambda_i^{(1)'} \equiv \Lambda_i^{(1)} - \langle \Lambda_i^{(1)} \rangle$ and $\Delta w_i^{2'} \equiv \Delta w_i^2 - \langle \Delta w_i^2 \rangle$. In all cases F1, F2 and F3, and
 524 at times after the similarity regime, the first term on the right hand side of equation (4.2)
 525 dominates over the second term and contributes the most to $\langle P_\Delta \rangle$ (see figure 8). During
 526 the part of the similarity regime when $\langle E_\Delta \rangle$ grows exponentially, $\beta \equiv \langle P_\Delta \rangle_{\text{Ave}} / \langle P_\Delta \rangle$ is
 527 constant in time and so is $1 - \beta = \langle P_\Delta \rangle_{\text{Fluc}} / \langle P_\Delta \rangle$ (see insets of figure 8): β is a constant
 528 equal to 0.53 ± 0.02 for F1 and F2 and equal to a slightly different value 0.66 ± 0.02 for F3
 529 where the Taylor length-based Reynolds number is significantly lower than for F1 and F2.
 530 One may indeed expect the fluctuation contribution $\langle P_\Delta \rangle_{\text{Fluc}}$ to increase in magnitude with
 531 increasing Reynolds number relative to the mean contribution $\langle P_\Delta \rangle_{\text{Ave}}$ in equation (4.2), and
 532 β to therefore be a decreasing function of Reynolds number.

533 Defining $\gamma_i^{(1)} \equiv \Lambda_i^{(1)} / \sqrt{\left\langle \left| S_{ij}^{(1)} \right|^2 \right\rangle}$ (where $|S_{ij}| \equiv \sqrt{S_{ij} S_{ij}}$) and $\theta_i \equiv \Delta w_i^2 / 2 \langle E_\Delta \rangle$, and

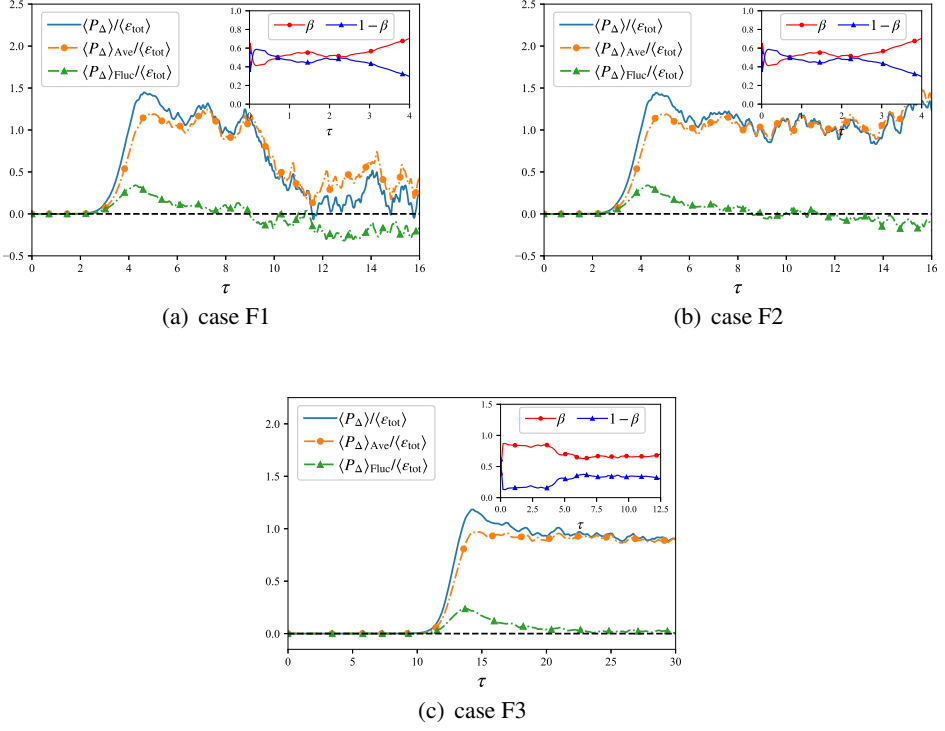


Figure 8: Time evolution of $\langle P_\Delta \rangle$ and its decomposition into average and fluctuation parts for different cases. Inset: the early-time evolution of the ratio of average term/total production and fluctuation term/total production.

534 using $\beta \equiv \langle P_\Delta \rangle_{\text{Ave}} / \langle P_\Delta \rangle$, we have

$$535 \quad \langle P_\Delta \rangle = -2 \frac{\sum_{i=1}^3 \langle \gamma_i^{(1)} \rangle \langle \theta_i \rangle}{\beta} \sqrt{\langle |S_{ij}^{(1)}|^2 \rangle} \langle E_\Delta \rangle. \quad (4.3)$$

536 We now examine the behaviours of $\langle \gamma_i^{(1)} \rangle$ and $\langle \theta_i \rangle$.

537 We start with $\langle \gamma_i^{(1)} \rangle$ which, unlike β and $\langle \theta_i \rangle$, are properties of the reference field and
 538 not of the velocity-difference field: $\langle \gamma_i^{(1)} \rangle$ are the average strain rates along the principal
 539 axes of the reference field's strain rate tensor and they are plotted versus time in figure 9.
 540 Note the constraints $\sum_{i=1}^3 \langle \gamma_i^{(1)} \rangle = 0$ and $\sum_{i=1}^3 \langle \gamma_i^{(1)2} \rangle = 1$. In cases F1 and F2, where the
 541 reference flow is statistically stationary, $\langle \gamma_i^{(1)} \rangle$ are constant in time and $\langle \gamma_1^{(1)} \rangle : \langle \gamma_2^{(1)} \rangle :$
 542 $\langle \gamma_3^{(1)} \rangle \approx -0.65 : 0.12 : 0.53$ in agreement with Betchov (1956)'s theoretical demonstration
 543 that there must be one principal axis direction which is compressive on average and two
 544 which are on average stretching. In case F3, the reference flow is not statistically stationary
 545 till about $\tau = 9.4$ but $\langle \gamma_i^{(1)} \rangle$ acquire a stable value before that and are already constant
 546 during the similarity period $\tau \approx 5.8$ to $\tau \approx 12.60$ (see figure 9(c)). In case F3, we observe

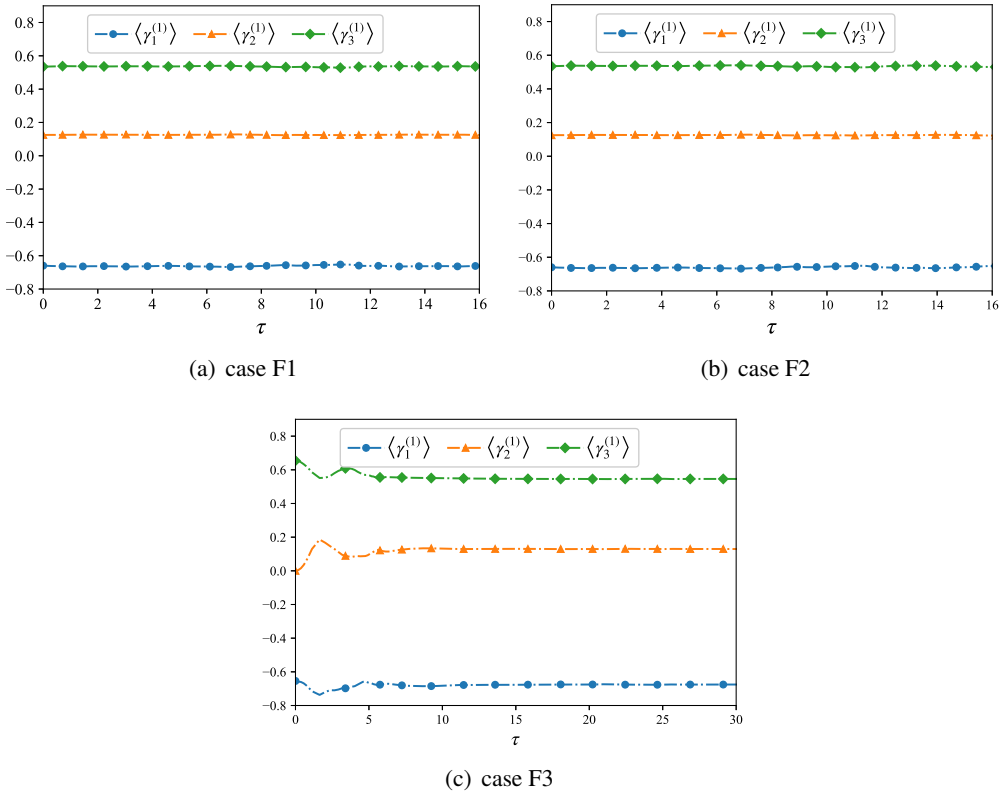


Figure 9: Time evolution of $\langle \gamma_i \rangle$ in the reference flows for different cases.

547 $\langle \gamma_1^{(1)} \rangle : \langle \gamma_2^{(1)} \rangle : \langle \gamma_3^{(1)} \rangle \approx -0.68 : 0.13 : 0.55$, which is very close to F1 and F2, also in
 548 agreement with Betchov (1956)'s prediction.

549 The average uncertainty energy $\langle E_\Delta \rangle$ consists of three average uncertainty energies
 550 $\langle \Delta w_i^2 / 2 \rangle$ in the principal axes of the reference field's strain rate tensor: $\langle E_\Delta \rangle = \sum_{i=1}^3 \langle \Delta w_i^2 / 2 \rangle$.
 551 The ratios $\langle \theta_i \rangle$ represent the proportion of average uncertainty energy in each principal
 552 direction and they of course sum up to 1. Their time evolution is shown in figure 10. Most
 553 of the uncertainty energy is concentrated in the compressive direction until $\tau \approx 8 - 9$ in
 554 cases F1 and F2 and for all time in case F3, in agreement with our observation at the
 555 end of subsection 2.2 that the production of uncertainty occurs by compressive motions.
 556 At saturation times there is a tendency for equipartition of average uncertainty energy in
 557 the three principal directions, in particular for F1 where the reference and principal fields
 558 completely decorrelate in the long term. The tendency remains for F2 and F3 but the average
 559 uncertainty energy in the most stretching direction remains significantly below the average
 560 uncertainty energy in the other two directions thereby ensuring that $\langle P_\Delta \rangle$ remains positive and
 561 the reference and perturbation fields remain partially correlated during eventual saturation.

562 In all three cases F1, F2 and F3, $\langle \theta_i \rangle$ are approximately constant during the similarity
 563 regime where β is also constant in time. During the similarity regime, the $\langle \theta_i \rangle$ values are
 564 $\langle \theta_1 \rangle : \langle \theta_2 \rangle : \langle \theta_3 \rangle \approx 0.58 : 0.19 : 0.23$ for cases F1 and F2 and $\langle \theta_1 \rangle : \langle \theta_2 \rangle : \langle \theta_3 \rangle \approx 0.59 : 0.18 : 0.23$
 565 for case F3. The values of $\langle \theta_i \rangle$ appear to be universal during the similarity regime
 566 whereas β seems to be dependent on Reynolds number.

567 Finally we discuss the relation between $\langle \varepsilon_\Delta \rangle$ and $\langle P_\Delta \rangle$. The self-similar uncertainty

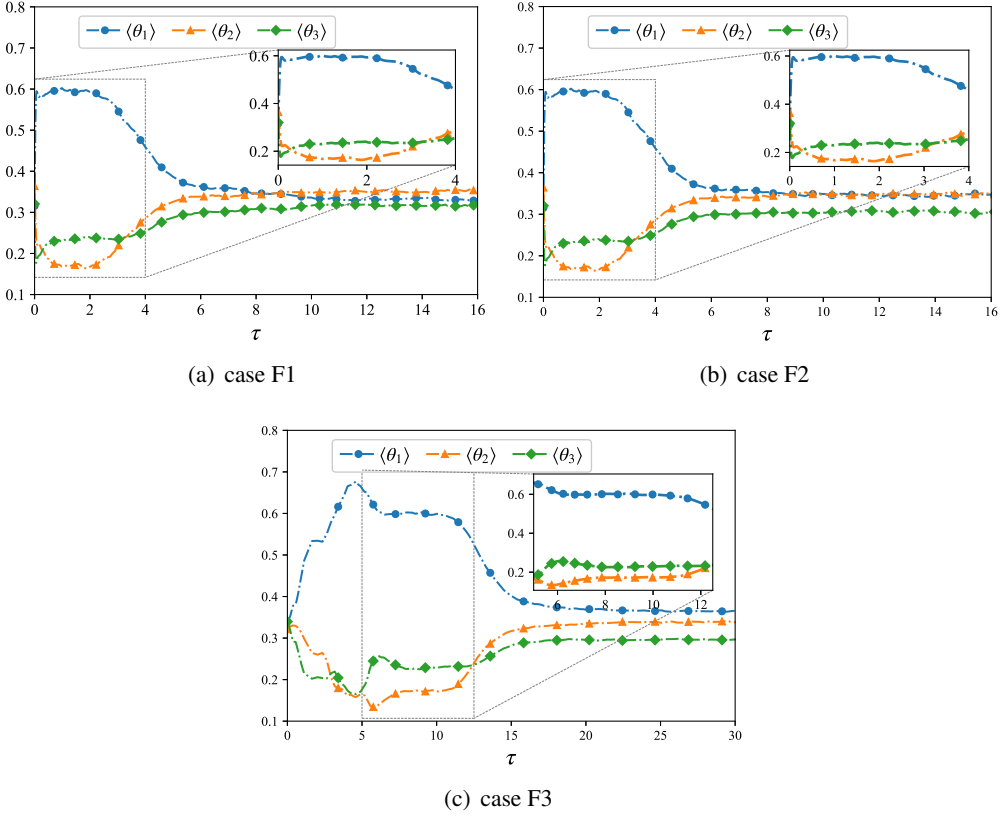


Figure 10: Time evolution of $\langle \theta_i \rangle$ for different cases. Inset: the time evolution of $\langle \theta_i \rangle$ during the similarity regime.

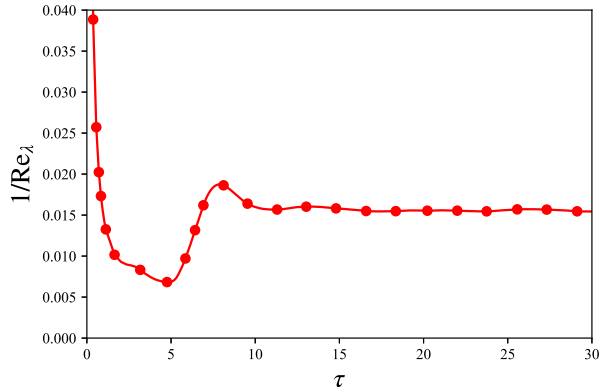


Figure 11: Time evolution of $1/\text{Re}_\lambda$ in case F3.

568 spectrum $\hat{E}_\Delta(k, t) = \langle E_\Delta \rangle L_\Delta f(kL_\Delta)$ implies that the uncertainty dissipation is

569
$$\langle \varepsilon_\Delta \rangle = 2\nu \int k^2 \hat{E}_\Delta(k) dk = 2\nu \langle E_\Delta \rangle L_\Delta \int k^2 f(kL_\Delta) dk = 2\nu \frac{\langle E_\Delta \rangle}{L_\Delta^2} \int x^2 f(x) dx, \quad (4.4)$$

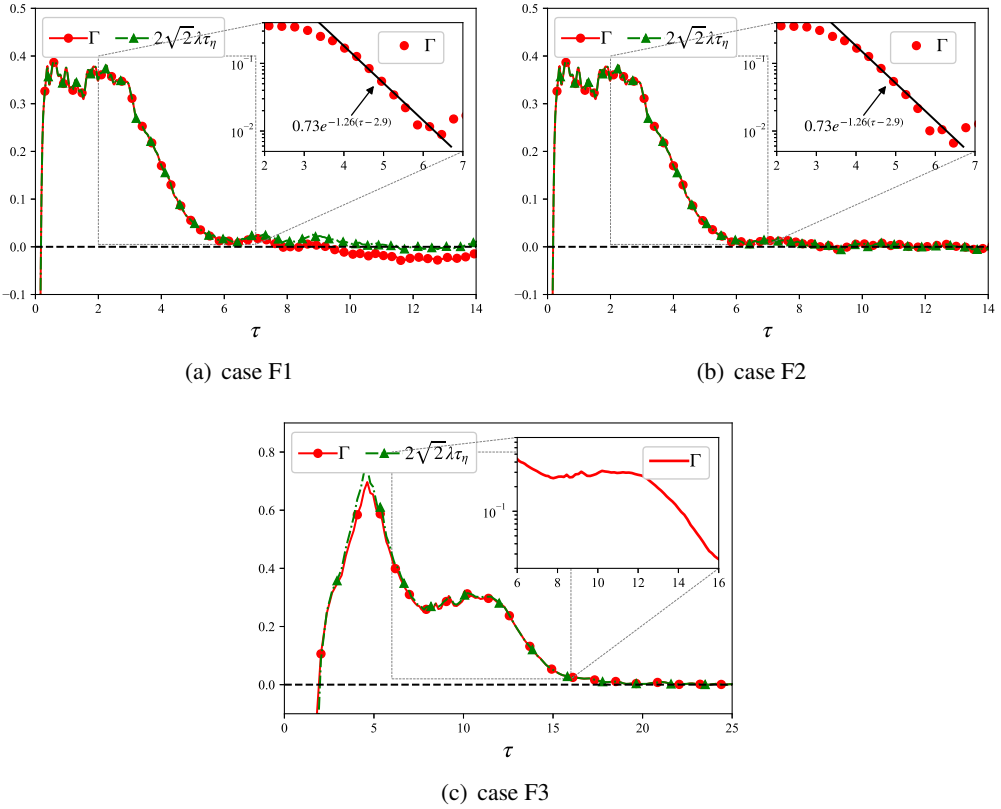


Figure 12: Time evolution of Γ and $2\sqrt{2}\lambda\tau_\eta$ for different cases. Inset: the time evolution of Γ during the similarity regime in semilogarithmic plot. The exponential function fit is indicated by a dash-dot line for F1 and F2.

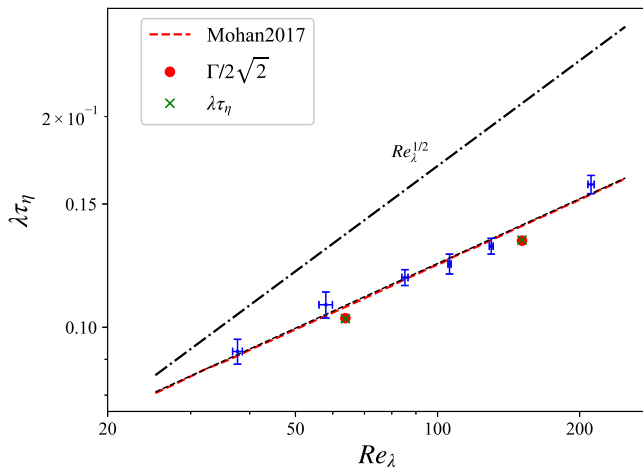


Figure 13: Schematic log-log plot of $\lambda\tau_\eta$ with the Taylor length-based Reynolds number Re_λ according to the numerical results (in blue) and models calibrated with Bayesian inference (in red) of Mohan *et al.* (2017). The Lyapunov exponents and the coefficient Γ obtained in the present work (in green crosses and red points) are also plotted.

570 where $\int x^2 f(x) dx$ is a time-constant. Defining $\alpha \equiv \langle \varepsilon_\Delta \rangle / \langle P_\Delta \rangle$, we obtain, from equation
 571 (4.3) and (4.4)

$$572 \quad \alpha = - \left[\frac{\beta \int_x x^2 f(x) dx}{\sum_{i=1}^3 \langle \gamma_i^{(1)} \rangle \langle \theta_i \rangle} \right] \frac{\nu}{L_\Delta^2 \sqrt{\langle |S_{ij}^{(1)}|^2 \rangle}}. \quad (4.5)$$

573 As shown above in this sub-section, the term in square brackets in equation (4.5) is constant
 574 in time. Figure 7 suggests that L_Δ and $l_\lambda^{(1)}$ have the same dependence on time but not the same
 575 dependence on viscosity. Therefore, the time dependence of $\left(L_\Delta^2 \sqrt{\langle |S_{ij}^{(1)}|^2 \rangle} \right)$ is the same as
 576 the time dependence of $\left((\eta^{(1)})^2 (\tau_\eta^{(1)})^{-1} \text{Re}_\lambda^{(1)} \right) \sim \text{Re}_\lambda^{(1)}$. For cases F1 and F2, the reference
 577 field, and therefore $\text{Re}_\lambda^{(1)}$ are statistically steady, and it therefore follows from equation (4.5)
 578 that α is constant in time during the similarity regime. For the same reason, α is constant
 579 in time after $\tau = 9.4$ in the similarity regime of case F3 because this is when the reference
 580 flow reaches the statistically steady state. During $\tau \in [7.5, 9.4]$ for F3, $1/\text{Re}_\lambda^{(1)}$ decreases
 581 monotonically from 0.0187 to 0.0156 as shown in figure 11. This 20% decrease is small
 582 compared to the variations of $1/\text{Re}_\lambda^{(1)}$ at normalised times τ smaller than 7.5 and results in a
 583 small decrease of α in the corresponding time period (i.e. a slow increase of $1/\alpha$, as shown
 584 in figure 3). Therefore, α can be considered to be approximately constant in the similarity
 585 period $\tau \in [7.5, 12.5]$ of F3.

586 We have seen at the end of subsection 4.1.2 and figure 3 that $\alpha = \langle P_\Delta \rangle / \langle \varepsilon_\Delta \rangle$ seems
 587 to be independent of viscosity but we also noted two paragraphs above that β is not. The
 588 dependencies on viscosity of $\beta\nu$ and $\left(L_\Delta^2 \sqrt{\langle |S_{ij}^{(1)}|^2 \rangle} \right)$ in equation (4.5) must therefore be the
 589 same and cancel each other.

590 Substituting equations (4.3) and equation (4.5) into equation (4.1), we obtain

$$591 \quad \frac{d}{dt} \langle E_\Delta \rangle = \Gamma \sqrt{\langle |S_{ij}^{(1)}|^2 \rangle} \langle E_\Delta \rangle, \quad (4.6)$$

592 where

$$593 \quad \Gamma = -2 \frac{1 - \alpha}{\beta} \sum_{i=1}^3 \langle \gamma_i^{(1)} \rangle \langle \theta_i \rangle. \quad (4.7)$$

594 This is a general rewriting of equation (4.1) with particularly interesting consequences for
 595 the similarity regime when α , β , $\langle \gamma_i^{(1)} \rangle$ and $\langle \theta_i \rangle$ are constant in time. The dimensionless
 596 coefficient Γ defined by equation (4.7) is therefore constant in time during the similarity
 597 regime but may depend on Reynolds number (i.e. viscosity) via the dependence of β on
 598 Reynolds number.

599 Looking at equation (4.6), an exponential growth of $\langle E_\Delta \rangle$ with a well-defined Lyapunov
 600 exponent λ can be derived during the similarity regime because Γ is constant in time:

$$601 \quad 2\lambda = \Gamma \sqrt{\langle |S_{ij}^{(1)}|^2 \rangle} = \frac{1}{\sqrt{2}} \Gamma \tau_\eta^{-1}. \quad (4.8)$$

602 The exponential growth of average uncertainty energy is, therefore, a consequence of
 603 similarity. How similarity (time-independent α , β , $\langle\theta_i\rangle$) and self-similar evolution of the
 604 uncertainty spectrum in terms of $\langle E_\Delta\rangle$ and L_Δ) may be a consequence of the presence of
 605 a strange attractor is, however, beyond this paper's scope but the question is now posed for
 606 future investigations.

607 The dimensionless coefficient Γ obtained from equation (4.7) and the Lyapunov exponent
 608 directly obtained from equation (1.1) are plotted in figure 12: for all cases F1, F2 and F3, Γ is
 609 about constant in the time range where exponential growth is present. The actual value of Γ in
 610 this time range is the same for F1 and F2 but it is different for F3 which has a lower Reynolds
 611 number. The scaling $\lambda\tau_\eta \sim \Gamma(\text{Re})$ suggests that the Lyapunov exponent may not scale with
 612 the Kolmogorov time τ_η (as claimed by Ruelle (1979)) if Γ depends on Reynolds number,
 613 which it may do on account of a Reynolds number dependence of β . The coefficient Γ , as
 614 well as the Lyapunov exponent, are also plotted in figure 13 to compare with previous data by
 615 Mohan *et al.* (2017). The ratio of Γ values in the F1 and F3 cases is $\Gamma_{\text{F1}}/\Gamma_{\text{F3}} = 1.29$ during
 616 the exponential growth time range, while $\beta_{\text{F3}}/\beta_{\text{F1}} = 1.25$ in the same regime. The data of
 617 Mohan *et al.* (2017) lead to $\Gamma_{\text{F1}}/\Gamma_{\text{F3}} \approx 1.30$ purely on the basis of the Reynolds numbers of
 618 F1 and F3 (see figure 13). This confirms the hypothesis that the different values of Γ in F1
 619 and F2 on the one hand and F3 on the other are caused by the difference in Reynolds number
 620 and nothing else.

621 The regime of approximate constancy of Γ is followed by a time range $\tau \in [2.9, 6.5]$
 622 where Γ appears to decay exponentially in the F1 and F2 cases (it is not clear whether such
 623 a range does or does not exist in the F3 case), see figure 12. Specifically, the exponential
 624 curve fit gives $\Gamma = 0.73 \exp(-1.26(\tau - 2.9))$. Using $\langle E_{\text{tot}}\rangle$ and $\langle T^{(1)}\rangle_t$ to non-dimensionalise
 625 equation (4.6), we write

$$626 \quad \frac{d}{d\tau} \frac{\langle E_\Delta\rangle}{\langle E_{\text{tot}}\rangle} = \Gamma \langle T^{(1)}\rangle_t \sqrt{\left\langle \left| S_{ij}^{(1)} \right|^2 \right\rangle} \frac{\langle E_\Delta\rangle}{\langle E_{\text{tot}}\rangle}. \quad (4.9)$$

627 For statistically stationary cases F1 and F2 we find $\langle T^{(1)}\rangle_t \sqrt{\left\langle \left| S_{ij}^{(1)} \right|^2 \right\rangle} = 12.77 \pm 0.56$ in the
 628 time range $\tau \in [2.9, 6.5]$. Therefore, equation (4.9) and our fitting of Γ imply $\langle E_\Delta\rangle / \langle E_{\text{tot}}\rangle \sim$
 629 $\exp(-9.32 \exp(-1.26(\tau - 2.9)))$, which is approximately consistent with the direct curve
 630 fitting in the inset of figure 1(d). Eventually Γ tends to 0 and the average uncertainty energy
 631 stops growing in all cases F1, F2 and F3.

632 4.2.2. Scaling of the Lyapunov exponent during similarity

633 Our analysis in section 4.2.1 and the data of (Mohan *et al.* 2017) presented in figure 13
 634 question the view that λ scales with τ_η (Ruelle 1979). If λ does not scale with τ_η which is the
 635 smallest Lagrangian time scale of the turbulence, it may scale with $\tau_E = \eta/U$, the shortest
 636 Eulerian time scale of the turbulence (Tennekes 1975), in which case $\lambda\tau_\eta \sim \tau_\eta/\tau_E \sim \text{Re}_\lambda^{1/2}$.
 637 The data of Mohan *et al.* (2017) in figure 13 suggests that λ grows faster than τ_η^{-1} but slower
 638 than τ_E^{-1} as Reynolds number increases, perhaps $\lambda \sim \tau_\eta^{-(1-c)/2} \tau_E^{-(1+c)/2}$, i.e. $\lambda\tau_\eta \sim \text{Re}_\lambda^{(1+c)/4}$,
 639 where $c \in (-1, 1]$. In fact, the results of Mohan *et al.* (2017) suggest that $\lambda\tau_\eta \sim \text{Re}_\lambda^{(1+c)/4}$
 640 where the most likely values of c are between 0 and 1/3. The large scale random sweeping
 641 of the smallest eddies represented in the Eulerian time scale τ_E appears to influence the
 642 growth of uncertainty even though the uncertainty exists only at the the smallest scales
 643 during the chaotic exponential growth. Interestingly, this large-scale random-sweeping effect
 644 is reflected in the decreasing dependence of β on Reynolds number (see equations (4.7)
 645 and (4.8)) which implies that $\langle P_\Delta\rangle$ should be increasingly dominated by $\langle P_\Delta\rangle_{\text{Fluc}}$ rather

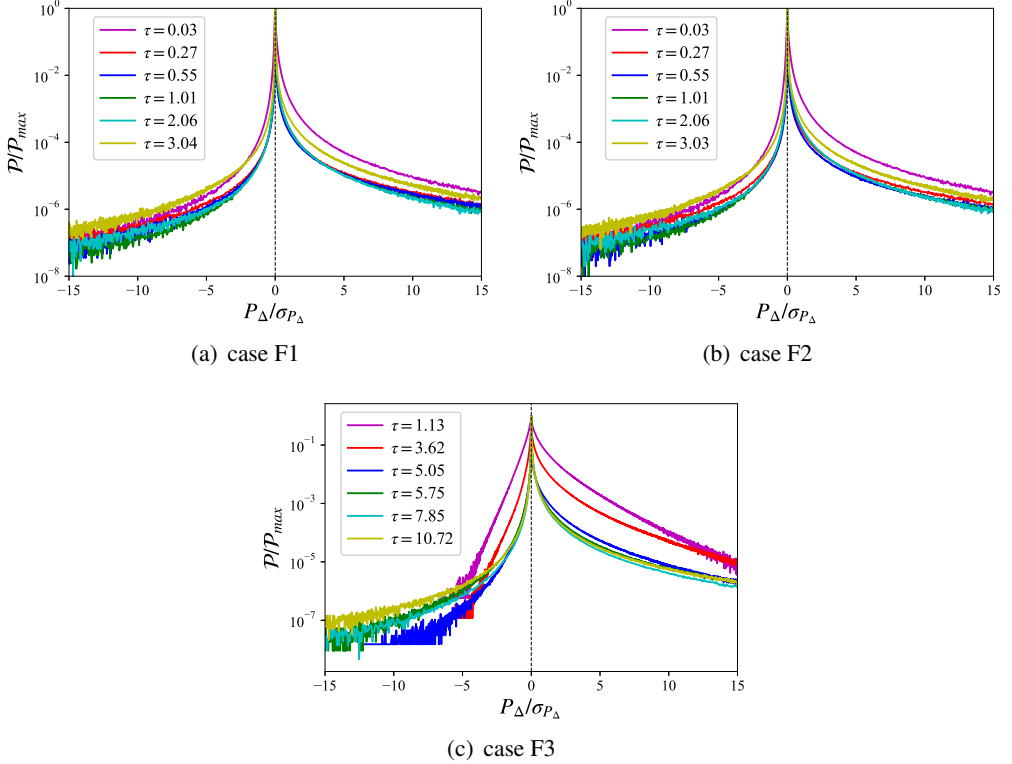


Figure 14: Early-time evolution of PDFs of P_Δ for different cases. PDFs are plotted versus $P_\Delta/\sigma_{P_\Delta}$ where σ_{P_Δ} is the standard deviation of P_Δ , defined as

$$\sigma_{P_\Delta}^2 \equiv \int_{P_{\Delta\min}}^{P_{\Delta\max}} (P_\Delta - \langle P_\Delta \rangle)^2 \mathcal{P}(P_\Delta) dP_\Delta.$$

646 than $\langle P_\Delta \rangle_{\text{Ave}}$ in equation (4.2) as Reynolds number increases. There seems to be a relation
 647 between large-scale random sweeping and uncertainty production, and in particular between
 648 random sweeping and the way that compression and stretching affect average uncertainty
 649 production either through average compression/stretching rates or through the correlations
 650 of their fluctuations with uncertainty energy fluctuations in specific stretching/compressive
 651 directions. A Lagrangian or some combined Eulerian-Lagrangian description of uncertainty
 652 (e.g. see Boffetta *et al.* (1997)) as advocated by Leith & Kraichnan (1972) in the introduction
 653 might have advantages over the present purely Eulerian approach as it may naturally account
 654 for the large-scale sweeping's effect on uncertainty and thereby return a reduced average
 655 uncertainty production. The large-scale sweeping's effect on uncertainty might also have
 656 some relation with the error in positions of local flow structures that Boffetta *et al.* (1997)
 657 identified.

658

4.3. The probability distribution of the uncertainty production

659 Even though the average uncertainty production rate is positive, the most likely value of P_Δ
 660 is zero at all times. In figures 14 and 15 we plot instantaneous probability density functions
 661 (PDF) of P_Δ sampled through all space and we examine how these PDFs evolve with time. An
 662 immediate observation is that the PDFs of P_Δ do not seem to match a well-known standard
 663 distribution (e.g. Gaussian, exponential, power-law) at any time and for any case F1, F2 and
 664 F3. Another immediate observation is that the early time PDFs of P_Δ for F3 differ from those

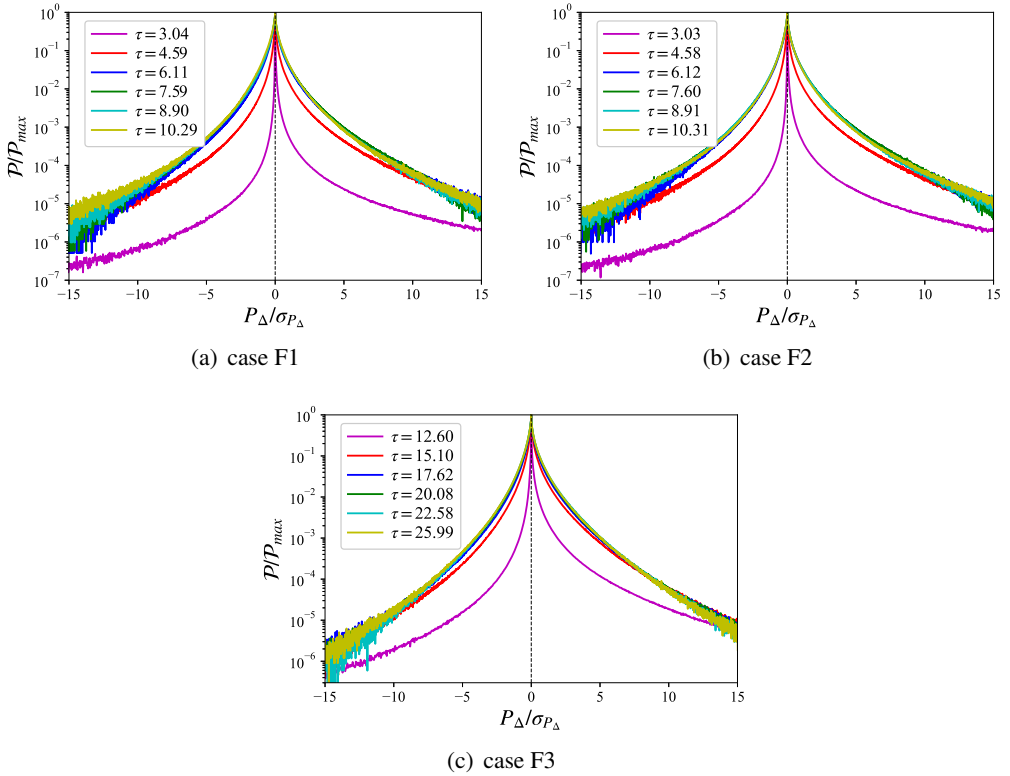


Figure 15: Evolution of PDFs of P_Δ after the similarity regime for different cases. PDFs are plotted versus $P_\Delta/\sigma_{P_\Delta}$ where σ_{P_Δ} is the standard deviation of P_Δ .

665 for F1 and F2 as their tails on the negative side are much shorter than on the positive side.
 666 These are times when the F3 reference flow is not statistically stationary.

667 Given that the most likely value of P_Δ is $P_\Delta = 0$, the non-zero values of $\langle P_\Delta \rangle$ result
 668 from the positive skewnesses and the heavy tails of these PDFs (see figures 14 and 15). The
 669 positive skewness and heavy tails, i.e. high kurtosis, set in from very early times and reveal
 670 an intermittent spatial distribution of co-existing uncertainty generation and depletion events
 671 where high generation events are more intense than high depletion events.

672 This spatial intermittency becomes increasingly acute and increasingly favourable to
 673 uncertainty generation rather than depletion events as the skewness and the kurtosis grow
 674 to extremely high positive values which fluctuate around a constant during the chaotic
 675 exponential growth in all F1, F2 and F3 cases (see figure 16). This happens within the
 676 similarity regime where α , β and θ_i are constant and the uncertainty spectrum is self-similar
 677 if scaled with $\langle E_\Delta \rangle$ and L_Δ . In fact, as shown in figure 14, the PDFs of P_Δ also approximately
 678 collapse during the time range of extreme skewness and kurtosis if normalised by the
 679 PDF's maximum value and standard deviation. During this time range where similarity and
 680 exponential uncertainty growth coexist, the kurtosis and the skewness fluctuate around 10^5
 681 and 200 respectively, suggesting that $\langle P_\Delta \rangle$ is predominantly determined by rare yet powerful
 682 events of uncertainty generation and depletion.

683 After the similarity and chaotic growth stage, both the skewness and the kurtosis of the
 684 PDFs continuously decrease with time indicating that more points in the flow participate in
 685 the uncertainty generation and depletion and in the overall value of $\langle P_\Delta \rangle$. The way these

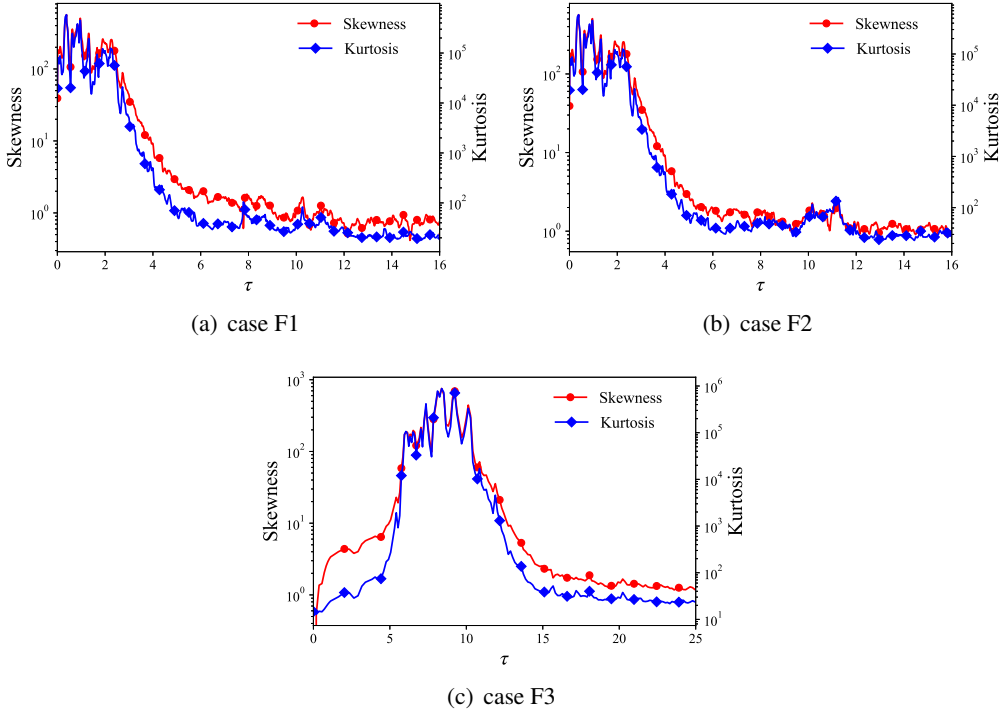


Figure 16: Time evolution of the sample kurtosis and skewness of PDF for different cases,

$$\text{which is defined as } K = \frac{\int_{P_{\Delta\min}}^{P_{\Delta\max}} (P_{\Delta} - \langle P_{\Delta} \rangle)^4 \varphi(P_{\Delta}) dP_{\Delta}}{\sigma_{P_{\Delta}}^4} \text{ and}$$

$$S = \frac{\int_{P_{\Delta\min}}^{P_{\Delta\max}} (P_{\Delta} - \langle P_{\Delta} \rangle)^3 \varphi(P_{\Delta}) dP_{\Delta}}{\sigma_{P_{\Delta}}^3}.$$

686 PDFs lead to the average values of P_{Δ} is subtle. The long time saturation value of $\langle P_{\Delta} \rangle$ is
 687 zero for F1 and non-zero for F2, yet the long time PDFs of P_{Δ} are similar in both cases, as
 688 are the long time values of kurtosis and skewness.

689 5. Conclusion

690 In the present work, we obtained the evolution equation (2.4) for the average uncertainty
 691 energy $\langle E_{\Delta} \rangle(t)$ in three-dimensional, incompressible and periodic/homogeneous Navier-
 692 Stokes turbulence. The average uncertainty energy evolves because of internal production,
 693 dissipation and external input/output of uncertainty. The internal production of uncertainty
 694 is a transfer from the correlation between the reference and perturbed fields to the average
 695 uncertainty energy and is determined by the eigenvalues of reference field's strain rate
 696 tensor and the distribution of uncertainty energy along its three eigenvectors. As shown by
 697 equation (2.12), stretching events decrease uncertainty while the compression events increase
 698 uncertainty.

699 We used DNS of periodic Navier-Stokes turbulence to study the gradual decorrelation
 700 process of two initially highly correlated flows. Three different DNS were run, F1, F2 and
 701 F3: two where the perturbation is seeded to a statistically stationary turbulence and where the
 702 forcing does (F1) or does not (F2) contribute directly to the progressive decorrelation between
 703 the reference and perturbed fields; and one (F3) where the reference and perturbed fields

704 are both initially very weak and grow together to eventually become statistically stationary
 705 without the external forcing contributing directly to their gradual decorrelation. In all three
 706 cases and at times when $\langle E_\Delta \rangle(t)$ is still small, a similarity time-range was found where the
 707 growth of the uncertainty spectrum is self-similar if scaled by $\langle E_\Delta \rangle(t)$ and the characteristic
 708 length $L_\Delta(t)$ of uncertainty, and where all the following quantities are constant in time: (i)
 709 the ratio α of average uncertainty dissipation to average uncertainty production, (ii) the ratio
 710 β characterising how much of the average uncertainty production rate is accountable to the
 711 average around which it fluctuates in space, and (iii) the distribution of uncertainty energy
 712 in the three eigen-directions of the reference field's strain rate tensor. These three similarity
 713 constancies and the constancy in time of the three average eigenvalues of the reference field's
 714 strain rate tensor imply an exponential growth in time for $\langle E_\Delta \rangle$ with Lyapunov exponent
 715 $\lambda \sim \Gamma \tau_\eta^{-1}$. The dimensionless coefficient Γ is given by equation (4.7) and grows with
 716 Reynolds number because β decreases with Reynolds number. This exponential growth for
 717 $\langle E_\Delta \rangle$ is observed in the earlier part of the time range of the similarity regime when the PDF
 718 of P_Δ collapses for different times if scaled by its maximum value and standard deviation.
 719 As a result, the kurtosis and skewness of this PDF are about constant in this time range. In
 720 fact, the value of this constant kurtosis is extremely large indicating extreme intermittency
 721 of P_Δ . The value of the constant skewness is also large and positive indicating that rare high
 722 uncertainty generation events are more intense than rare high uncertainty depletion events.
 723 The average value of P_Δ is controlled by this intermittency in this time range. Note that the
 724 most probable value of P_Δ is zero at all times.

725 During the chaotic exponential growth regime, the ratio of L_Δ to l_λ is roughly constant. In
 726 agreement with previous observations (Mohan *et al.* 2017), the Lyapunov exponent does not
 727 scale with the Kolmogorov time τ_η , but it also does not scale with the smallest Eulerian time
 728 scale τ_E (Tennekes 1975). It appears to depend on both as $\lambda \sim \tau_\eta^{-(1-c)/2} \tau_E^{-(1+c)/2}$ with c
 729 between 0 and 1/3, implying that large scale random sweeping of the smallest length-scales
 730 influences the growth of uncertainty even though uncertainty only exists in the smallest
 731 eddies in the time range of chaotic exponential growth.

732 The chaotic growth time-range is followed by a time-range in the F1 and F2 cases where
 733 Γ decays exponentially and $\langle E_\Delta \rangle$ grows as an exponential of an exponential. In turn, this
 734 exponential of exponential time-range may be followed by a linear time range in the F1 case
 735 consistently with previous DNS studies (Berera & Ho 2018; Boffetta & Musacchio 2017),
 736 but not in the F2 case, at least for our present DNS Reynolds numbers. The linear growth
 737 of uncertainty seems to be sensitive to the direct presence (F1) or absence (F2) of external
 738 forcing in the evolution of $\langle E_\Delta \rangle$. We did not detect a linear time growth of $\langle E_\Delta \rangle$ in F3 either,
 739 however the F3 Reynolds number is even lower.

740 Finally, the exponential growth of $\langle E_\Delta \rangle$ is usually attributed to the presence of a strange
 741 attractor whereas it has been obtained here from similarity. Future research should attempt to
 742 shed light on the relations between similarity and strange attractors, and on how similarity may
 743 be a consequence of the presence of a such an attractor and underlying chaos. Future research
 744 may also consider how this paper's approach to uncertainty in homogeneous turbulence can
 745 be extended to a wider range of turbulent flows. In general, the governing equation for Navier-
 746 Stokes uncertainty is (2.3) rather than (2.4). Hence, turbulent as well as viscous diffusion
 747 and also pressure effects will need to be taken into account explicitly in the evolution
 748 of uncertainty. Various boundary conditions and errors on boundary conditions in case of
 749 complex turbulent flows will also be an issue, not to mention various body forces and the
 750 presence in many turbulent flows of turbulent/non-turbulent or turbulent/turbulent or other
 751 (e.g. density) interfaces. The identification of local compression and stretching events as key
 752 to the development of uncertainty means that future prediction methods may benefit from

Case	$\langle E_{\Delta}(t_0) \rangle / \langle E_{\text{tot}}(t_0) \rangle$	Perturbed range
Standard (F1 or F2)	8.077×10^{-6}	$[0.9k_{\text{max}}, 1.0k_{\text{max}}]$
K08K09	8.077×10^{-6}	$[0.8k_{\text{max}}, 0.9k_{\text{max}}]$
K07K08	8.077×10^{-6}	$[0.7k_{\text{max}}, 0.8k_{\text{max}}]$
Amp01	8.077×10^{-7}	$[0.9k_{\text{max}}, 1.0k_{\text{max}}]$

Table 3: Numerical configurations for different cases. The two standard cases correspond to F1 and F2 in the manuscript. There are two cases K08K09, one for F1 and one for F2, and similarly for cases K07K08 and Amp01. For the standard F1 and F2 cases, the initial perturbations are generated randomly under constraints (1), (2) and (3) mentioned in section 3, but for the other six cases the initial perturbations are generated partially randomly under constraints (1) and (2) in order to precisely control the initial uncertainty energy.

753 strategies for early detection of such events so as to concentrate maximum accuracy on the
754 compression events and less accuracy on the stretching events. However, the roles of all the
755 other aforementioned effects should not be underestimated and future research is needed to
756 show whether they are subdominant or not and in which flows.

757 **Acknowledgements.** Jin Ge acknowledges financial support from the China Scholarship Council. We are
758 grateful for the access to the computing resources supported by the Zeus supercomputers (Mésocentre de
759 Calcul Scientifique Intensif de l’Université de Lille).

760 **Funding.** This research received no specific grant from any funding agency, commercial or not-for-profit
761 sectors.

762 **Declaration of interests.** The authors report no conflict of interest.

763 Appendix A. Sensitivity of the uncertainty energy to the initial perturbation

764 To investigate the sensitivity of the evolution of average uncertainty energy to the initial
765 perturbation, a series of simulations have been executed, of which the configurations are
766 presented in table 3. By checking the evolution of the average uncertainty energy, the
767 influence of the perturbed range (cases “standard”, “K07K08” and “K08K09”) and of the
768 amplitude (cases “standard” and “Amp01”) of the initial perturbation is investigated. During
769 the similarity period, the changes in the amplitude and the perturbed range have very little
770 effect on the evolution of the average uncertainty energy, other than giving the evolution an
771 offset (explained below). At late times, the difference between average uncertainty energies
772 induced by different initial perturbations becomes more obvious for F1 where the external
773 forcing causes an eventual decorrelation between the perturbed and the unperturbed velocity
774 fields.

775 Figure 17 presents the time evolutions of the average uncertainty energy for different per-
776 turbed wavenumber ranges. A higher wavenumber perturbed range implies higher uncertainty
777 dissipation rate for the seeded uncertainty at the earliest times, which causes lower value of
778 $\langle E_{\Delta} \rangle / \langle E_{\text{tot}} \rangle$ at very early times and during the similarity period. The effect appears in the
779 log-linear inset of figure 17 as a vertical offset of the curves for the different cases. The average
780 uncertainty energy grows exponentially in all three cases with the same Lyapunov exponent.
781 These different vertical offsets lead to slightly different exit times from the similarity regime.
782 The regime of exponential growth is followed by what appears to be an exponential of
783 exponential regime, where the difference of wavenumber perturbed range has little influence

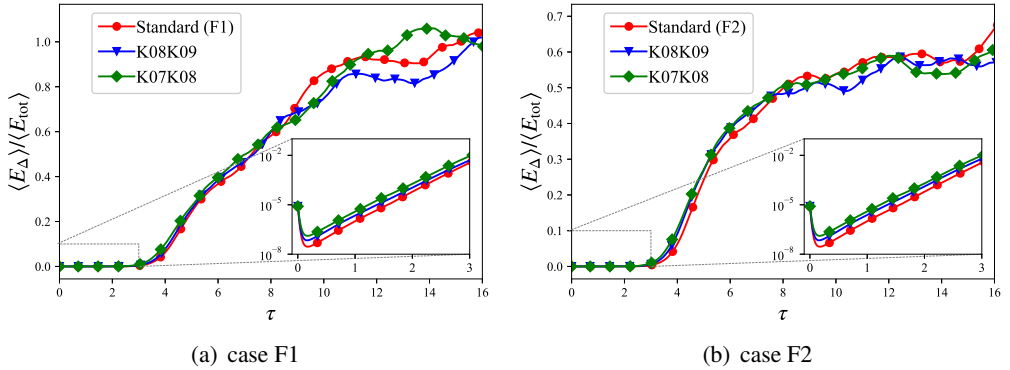


Figure 17: Time evolution of average uncertainty energy with different perturbed wavenumber range. Inset: the initial time evolution of average uncertainty energy in semilogarithmic plot.

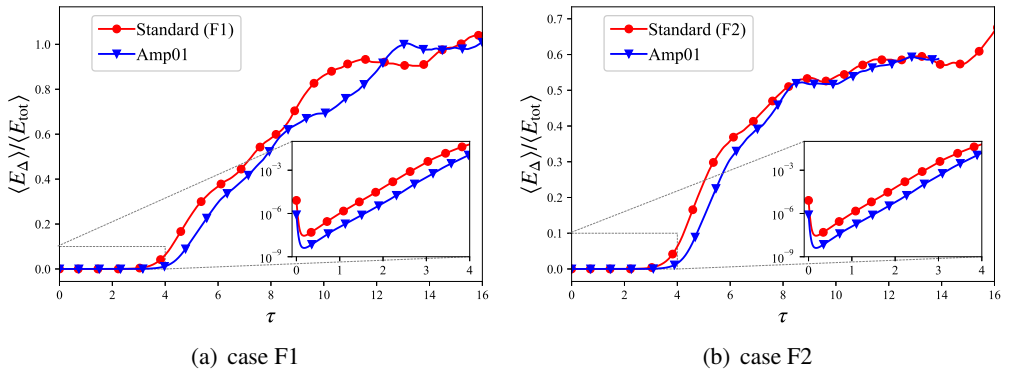


Figure 18: Time evolution of average uncertainty energy with different initial uncertainty energy. Inset: the initial time evolution of average uncertainty energy in semilogarithmic plot.

784 on the evolution of average uncertainty energy since the lines in figure 17 are very close to
 785 each other albeit with a persisting small offset.

786 Figure 18 presents the time evolution of the average uncertainty energy for the different
 787 initial uncertainty energy levels. As can be seen in the figure, the change in the amplitude
 788 of initial perturbation has the same effect as the change in the perturbed wavenumber range,
 789 i.e., no significant influence on the evolution of uncertainty energy other than creating an
 790 offset.

791 We also checked the uncertainty spectra in the self-similar regime for our various cases
 792 with different initial perturbations, as shown in figure 19. All the self-similar spectra with
 793 different initial perturbations collapse together.

794 As an overall conclusion, the early- and mid-time evolutions of the average uncertainty
 795 energy are not very sensitive to the form and amplitude of the initial perturbations, other
 796 than giving the evolution an offset.

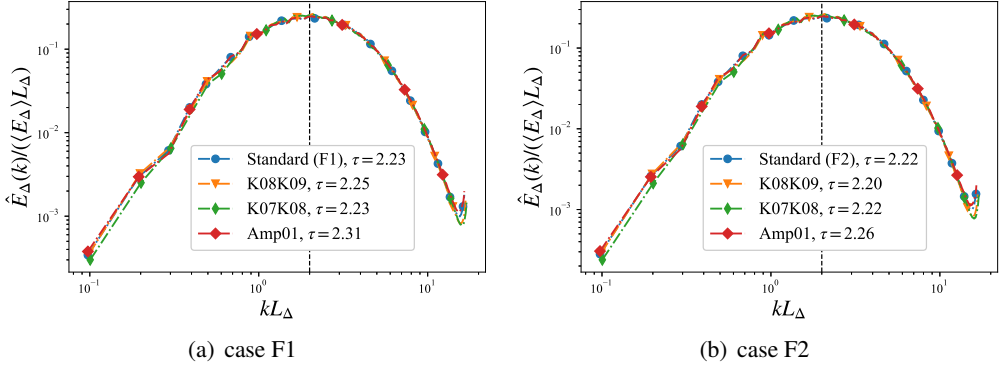


Figure 19: Uncertainty energy spectra in the similarity regime. The spectra are normalized by $\langle E_\Delta \rangle$ and L_Δ .

Case	N^3	ν	$\langle \langle \varepsilon \rangle \rangle_t$	$\langle U \rangle_t$	$\langle L \rangle_t$	$\langle T_0 \rangle_t$	$\langle \text{Re} \rangle_t$	$\langle \text{Re}_\lambda \rangle_t$	$\langle k_{\max} \eta \rangle_t$
F4	128^3	0.0060	0.0996	0.598	1.197	2.003	119.2	56.7	1.61

Table 4: Parameters of the reference flows for case F4.

797 Appendix B. Reynolds-number dependence of the time range of the exponential 798 regime

799 To investigate the relation between the time range of the exponential regime and the Reynolds
800 number, we have run another simulation which has the same external forcing as F2 with initial
801 perturbations which, like standard F1, F2 and F3, obey the three constraints mentioned in
802 section 3. Table 4 presents the main parameters of this extra case F4, as well as cases F2/F3
803 discussed in the manuscript. As shown in table 1 and table 4, the Taylor Reynolds number of
804 case F4 is close to that of case F3. Figure 20 presents the growths of average uncertainty in
805 a semilogarithmic plot. In figure 20(a) we compare the evolution in cases F2 and F4. As can
806 be seen in the figure, the exponential regime in F4 is longer than in F2, and also has a slower
807 growth rate than F2, which is (see equation (4.9))

$$808 \quad \Gamma \langle T^{(1)} \rangle_t \sqrt{\langle |S_{ij}^{(1)}|^2 \rangle} \sim \Gamma(\text{Re}_\lambda) \cdot \text{Re}_\lambda. \quad (\text{B } 1)$$

809 The lower Reynolds number case has a lower growth rate. Furthermore, as shown in figure
810 6, the exit time from the similarity regime corresponds to the moment when the velocities
811 at the largest wavenumbers become completely decorrelated, i.e. $\hat{E}_\Delta(k_{\max}) = \hat{E}_{\text{tot}}(k_{\max})$.
812 Therefore, as the Reynolds number increases, the energy spectrum's inertial range also
813 increases towards smaller scales, causing a decreasing threshold value $\langle E_\Delta \rangle / \langle E_{\text{tot}} \rangle$ that
814 needs to be overcome for the exit time from the exponential growth regime. As a result, the
815 lower Reynolds number case has a longer time-range of exponential growth.

816 In figure 20(b) we compare the exponential growths in cases F3 and F4. It is observed that
817 cases F3 and F4 have similar exponential growth rates. The slight difference in exponential
818 growth rates is caused by the small difference in Reynolds numbers. To verify this point,
819 equation (B 1) is applied, along with the observation of Mohan *et al.* (2017) that $\Gamma(\text{Re}_\lambda) \sim$

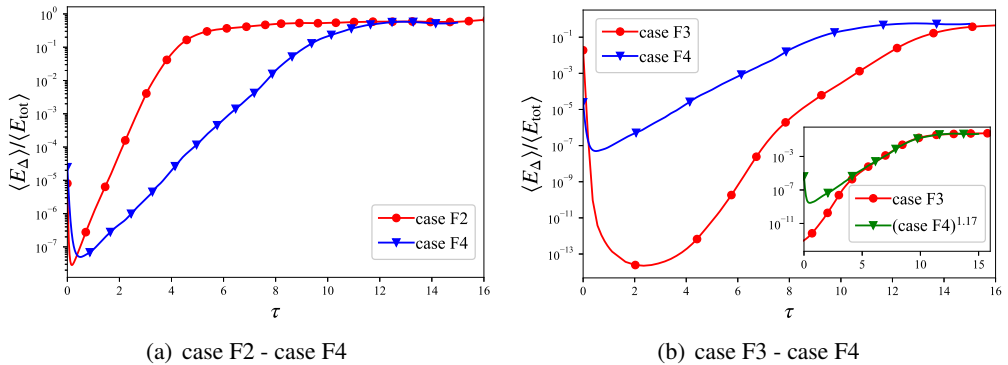


Figure 20: Time evolution of average uncertainty energy in semilogarithmic plot. In the inset of (b), we plot $(\langle E_{\Delta} \rangle / \langle E_{\text{tot}} \rangle)^{1.17}$ for F4 and $\langle E_{\Delta} \rangle / \langle E_{\text{tot}} \rangle$ for F3 translated in the horizontal axis by 2.7 τ -units to the left.

820 $\text{Re}_{\lambda}^{1/3}$. Therefore, we predict that the ratio of exponential growth rates of F3 and F4 is
 821 $(63.8/56.7)^{4/3} = 1.17$, which is verified by our simulations as shown in the inset of figure
 822 20(b). Although cases F3 and F4 have similar exponential growth rates, case F4 has a longer
 823 exponential regime. This may have something to do with the fact that F3 is not statistically
 824 stationary until $\tau = 9.3$ whereas F4 is statistically stationary from the start of the perturbation.

REFERENCES

- 825 ASHURST, W.T., KERSTEIN, A.R., KERR, R.M. & GIBSON, C.H. 1987 Alignment of vorticity and scalar
 826 gradient with strain rate in simulated Navier–Stokes turbulence. *Phys. Fluids* **30** (8), 2343–2353.
- 827 AURELL, E., BOFFETTA, G., CRISANTI, A., PALADIN, G. & VULPIANI, A. 1997 Predictability in the large: an
 828 extension of the concept of Lyapunov exponent. *J. Phys. A Math. Theor.* **30** (1), 1.
- 829 BATCHELOR, G. K. 1953 *The theory of homogeneous turbulence*. Cambridge university press.
- 830 BERERA, A. & HO, R.D.J.G. 2018 Chaotic properties of a turbulent isotropic fluid. *Phys. Rev. Lett.* **120** (2),
 831 024101.
- 832 BETCHOV, R. 1956 An inequality concerning the production of vorticity in isotropic turbulence. *J. Fluid
 833 Mech.* **1** (5), 497–504.
- 834 BOFFETTA, G., CELANI, A., CRISANTI, A. & VULPIANI, A. 1997 Predictability in two-dimensional decaying
 835 turbulence. *Phys. Fluids* **9** (3), 724–734.
- 836 BOFFETTA, G. & MUSACCHIO, S. 2017 Chaos and predictability of homogeneous-isotropic turbulence. *Phys.
 837 Rev. Lett.* **119** (5), 054102.
- 838 CHEUNG, P.Y. & WONG, A.Y. 1987 Chaotic behavior and period doubling in plasmas. *Phys. Rev. Lett.* **59** (5),
 839 551.
- 840 CLARK, D., ARMUA, A., FREEMAN, C., BRENER, D.J. & BERERA, A. 2021 Chaotic measure of the transition
 841 between two-and three-dimensional turbulence. *Phys. Rev. Fluids* **6** (5), 054612.
- 842 CLARK, D., ARMUA, A., HO, R.D.J.G. & BERERA, A. 2022 Critical transition to a non-chaotic regime in
 843 isotropic turbulence. *J. Fluid Mech.* **930**.
- 844 CRISANTI, A., JENSEN, M.H., VULPIANI, A. & PALADIN, G. 1993 Intermittency and predictability in
 845 turbulence. *Phys. Rev. Lett.* **70** (2), 166.
- 846 DEISSLER, R.G. 1986 Is Navier–Stokes turbulence chaotic? *Phys. Fluids* **29** (5), 1453–1457.
- 847 FRISCH, U. 1995 *Turbulence: The Legacy of AN Kolmogorov*. Cambridge University Press.
- 848 GOTO, S. & VASSILICOS, J.C. 2009 The dissipation rate coefficient of turbulence is not universal and depends
 849 on the internal stagnation point structure. *Phys. Fluids* **21** (3), 035104.
- 850 HO, R.D.J.G., ARMUA, A. & BERERA, A. 2020 Fluctuations of Lyapunov exponents in homogeneous and
 851 isotropic turbulence. *Phys. Rev. Fluids* **5** (2), 024602.
- 852 LEITH, C.E. 1971 Atmospheric predictability and two-dimensional turbulence. *J. Atmos. Sci.* **28** (2), 145–161.

- 853 LEITH, C.E. & KRAICHNAN, R.H. 1972 Predictability of turbulent flows. *J. Atmos. Sci.* **29** (6), 1041–1058.
- 854 LI, Y.C. 2014 The distinction of turbulence from chaos – rough dependence on initial data. *Electron. J.*
855 *Differ. Equ.* **2014** (104), 1–8.
- 856 LI, Y.C., HO, R.D.J.G., BERERA, A. & FENG, Z.C. 2020 Superfast amplification and superfast nonlinear
857 saturation of perturbations as a mechanism of turbulence. *J. Fluid Mech.* **904**.
- 858 LORENZ, E.N. 1963 Deterministic nonperiodic flow. *J. Atmos. Sci.* **20** (2), 130–141.
- 859 LORENZ, E.N. 1969 The predictability of a flow which possesses many scales of motion. *Tellus* **21** (3),
860 289–307.
- 861 MOHAN, P., FITZSIMMONS, N. & MOSER, R.D. 2017 Scaling of Lyapunov exponents in homogeneous isotropic
862 turbulence. *Phys. Rev. Fluids* **2** (11), 114606.
- 863 PAUL, I., PAPADAKIS, G. & VASSILICOS, J. C. 2017 Genesis and evolution of velocity gradients in near-field
864 spatially developing turbulence. *J. Fluid Mech.* **815**, 295–332.
- 865 RUELLE, D. 1979 Microscopic fluctuations and turbulence. *Phys. Lett., A* **72** (2), 81–82.
- 866 RUELLE, D. 1981 Small random perturbations of dynamical systems and the definition of attractors. *Commun.*
867 *Math. Phys.* **82**, 137–151.
- 868 SPARROW, C. 2012 *The Lorenz equations: bifurcations, chaos, and strange attractors*, , vol. 41. Springer
869 Science & Business Media.
- 870 TENNEKES, H 1975 Eulerian and Lagrangian time microscales in isotropic turbulence. *J. Fluid Mech.* **67** (3),
871 561–567.
- 872 TENNEKES, H. & LUMLEY, J.L. 1972 *A first course in turbulence*. MIT press.
- 873 VINCENT, A. & MENEGUZZI, M. 1991 The spatial structure and statistical properties of homogeneous
874 turbulence. *J. Fluid Mech.* **225**, 1–20.
- 875 YOFFE, S.R. 2012 Investigation of the transfer and dissipation of energy in isotropic turbulence. PhD thesis,
876 University of Edinburgh.